

Abstract

Acknowledgements

Contents

1	Introduction	7
2	Theory	11
2.1	Spin-orbit coupling	11
2.2	Wannier Functions	11
3	Charge order and spin-momentum locking in high spin-orbit coupled ferroelectrics	13
4	Spin-momentum locking in high spin-orbit coupled ferroelectrics	15
4.1	Introduction	15
4.2	Rashba-Bychkov Effect	16
4.3	Orbital Rashba Effect	18
4.3.1	Tight-Binding model	19
4.4	Overview: Germanium Telluride	23
4.5	Methods	23
4.6	Band structure	23
4.7	Results and Discussion	24
4.8	Conclusions	25
5	Coupling between spin and strain density waves	31
5.1	Introduction	31
5.2	Experimental methods	31
5.3	Theory	32
5.4	Results	33
6	Topological Multiferroic switching; coupling between Magnetism and Ferroelectricity in GdMn₂O₅	39
6.1	Introduction	39
6.2	Experimental results	42
6.3	Modeling	43
6.4	Simplified Model	47
7	Mechanical softening in Ferroelectric domain walls	53
7.1	Introduction	53
7.2	Experimental	53
7.3	Theory	54
7.4	Results	55

Chapter 1

Introduction

Theoretical condensed matter research is plagued by a fundamental issue of complexity. The shear amount of degrees of freedom in a material of any technologically relevant scale is overwhelming (i.e. $\sim 10^{23}$ electrons per cm^3), and make it impossible to describe the quantum mechanical wavefunction exactly [there is some more nice things along this line in Wen]. This forces researchers in the field to make approximations, as to make the problem tractable, while still capturing the essential physics resulting in the effects under investigation.

The way to make progress with this undertaking has always been to try and isolate the parts of the system that contribute the most. As is well known, every quantum mechanical system is governed fundamentally by its Hamiltonian. One could go so far as to say that if we would be able to exactly calculate all of its eigenvectors and eigenvalues, the field of condensed matter would be completed. This is of course impossible for reasons stated above.

The full Hamiltonian can be decomposed into several contributions, which allows one to focus on the most important contributions, while discarding the rest. For example, the elastic energy scales needed to completely break a material, while important for mechanical studies, are so much larger than those governing the movement of electrons through the material, that they can be discarded if we are only interested in the latter.

What this means fundamentally is that we are separating the full Hilbert space of possible states that the full wavefunction system can assume into separate parts that each take care of different aspects of the full physics. A relevant example is that the ionic response of a material can be described by phonons, these contribute very little to currents that may flow through it. Thus, while the full wavefunction and Hilbert space contains both the phonons and electrons, we can split it up into both parts, with an interaction between them. If this interaction is negligible, we can write the full wavefunction as the product of two parts in each of these spaces with no entanglement between them, and we can solve the physics of both parts separately.

If this procedure is carried out systematically, at some point we end up with something that is actually solvable, which will hopefully describe the biggest part of the observed behavior. This is essentially how the field of condensed matter has progressed starting from the most fundamental quantum mechanical laws, first focusing on exactly solvable constituent problems, gradually adding complexity in order to describe more complex physics.

In general, projects contained in this Thesis will focus on this step of taking two solved constituent problems, adding an interaction between them and observing what new physics emerge. There are three of these coupling interactions that will be discussed: spin-orbit coupling (SOC), exchange striction, and electrostriction. The focus will lie on electronic, magnetic and structural properties of ferroic crystals. In some of these materials, where multiple ferroic orders coexist (so-called multiferroics), the interactions will allow to influence either ferroic order by perturbing the other.

The SOC is a relativistic effect, that can often be ignored if one is interested in the electronic structure inside a crystal with light ions. In the case of GeTe, however, an anomalously large spin-splitting of two normally degenerate spin states, was found in the bandstructure of the ferroelectric material. Another result of this interaction is a fundamental coupling between the crystalline lattice and magnetism if it is present. This causes the usually isotropic magnetic interactions between the on-site spins, given by the Heisenberg exchange Hamiltonian $\sum_{\langle i,j \rangle} J_{ij} \mathbf{S}_i \cdot \mathbf{S}_j$, to become highly anisotropic, i.e. the coupling between the components of the spins depends on the direction of the bond: $\sum_{\langle i,j \rangle, \mu, \nu} J_{ij}^{\mu\nu} S_i^\mu S_j^\nu$ where $\mu, \nu = x, y, z$. We will investigate Sr₂IrO₄ in particular, where there is a strong SOC on the magnetic Ir atoms.

The second effect we will highlight is magnetic exchange striction, which stems from the dependence of exchange constants J_{ij} on structural distortions, leading to a coupling between the spins and phonons. This leads to a modulation of the magnetic configuration when phonons are present in the material, and vice versa to the creation of phonons when the magnetic interaction can gain energy if bond lengths are varied. Here we will highlight two specific situations. In the first, a ferroelectric polarization (a $\mathbf{k} = \mathbf{0}$ phonon) emerges due to geometric frustration of anti-ferromagnetic ordering in GdMn₂O₅. The second situation is the well-known coupling between the spin density wave and charge density wave in elemental Chromium. In this case a peculiar nesting of the Fermi-surfaces results in a spin density wave to be stabilized, whereupon the exchange striction creates a charge density wave. It is this interaction that opens the path to a very precise control in ultrafast photoexcitation experiments of these collective modes, where the excitation of the spin density wave causes in turn an excitation in the charge density wave. The latter can then be controlled very precisely by further pulses, as is demonstrated in our work.

Lastly, the interaction between strain and ferroelectricity will be carefully studied in 180° domain walls in BaTiO₃. This is one of the most well-known ferroelectric materials harboring a wide of ferroelectric phases, with very large polarization. Interestingly the coupling under discussion leads to a noticeable mechanical softening of 180° ferroelectric domain walls. This is not straightforward as the domain wall is not ferroelastic, i.e. it separates two domains with the same values for the strain tensor, making it not a priori clear why the purely ferroelectric wall appears softer. We will show that the electrostriction leads to a strain profile close to the wall which can interact with an atomic force microscopy tip, bending the wall towards it and thus appearing softer.

Aside from the purely academic interest, these interactions between separate parts of the systems also hold promise from a technological point of view. Due to these cross-couplings between degrees of freedom, as was alluded to before, it is possible to influence one part by perturbing the other. The most brought up case is that of hard disks, where the ferromagnetic domains that store the

data need to be reoriented by applying an external magnetic field, making it rather inefficient due to heating and limiting the data density caused by magnetic stray fields influencing multiple domains. If one would be able, however, to control the magnetic domains by applying an electric field, this would dramatically increase the efficiency. This is what makes multiferroics such as in our case GdMn_2O_5 , are so interesting. The coupling between the ferroelectric polarization and magnetization in the material causes one to be able to change the latter by applying an electric field to the former. A thorough understanding of the switching behavior in this material is of paramount importance to utilize this effect efficiently. In the case of GeTe, as will discussed later, the spin polarization of the bands closest to the fermi level depend the direction of the ferroelectric polarization, thus theoretically allowing for a Datta Das transistor [citation!], allowing only a particular spin-polarized current to flow through the material.

In the case of the ferroelectric domain walls, the cross-coupling between strain and ferroelectricity allows to effectively move the ferroelectric domains by applying a strain field through a tip, due to the presence of very soft sliding modes.

[rundown of chapters here]

Chapter 2

Theory

2.1 Spin-orbit coupling

2.2 Wannier Functions

In a lot of the work presented in this Thesis we construct models to describe the physics that result in a certain effect in real materials. These models are most of the time defined in terms of a limited set of local atomic-like orbitals, since these offer the most intuitive understanding most of the time, and the biggest contribution to particular effects can often be traced back to only a limited subset of all the orbitals.

If we want to apply these models to real materials to get not only qualitative, but also quantitative results, we need to perform a fit to either experimentally obtained values, or first-principles simulations. The most feasible way is usually the latter, which requires us to find a bridge between the plane waves that are used in a lot of first-principles DFT codes, and the localized basis set of that the model is built from.

Wannier functions offer a rigorous and flexible solution to this question, rewriting the Bloch functions as a discrete Fourier transform of (exponentially) localized, cell-periodic wavefunctions.

This construction is flexible in the sense that it is not unique. Bloch functions have a gauge freedom at each k value, which in turn will have an effect on the Wannier functions. One gauge that is commonly used is the one that localized the functions as much as possible, leading to the so-called Maximally Localized Wannier Functions (MLWF). Other gauges can be chosen such that the obtained functions have certain symmetries or have maximum similarity to atomic orbitals.

Chapter 3

Charge order and spin-momentum locking in high spin-orbit coupled ferroelectrics

Chapter 4

Spin-momentum locking in high spin-orbit coupled ferroelectrics

4.1 Introduction

The research field of spintronics aims to understand the behavior of spins inside materials, and translate this understanding into active control of these degrees of freedom for possible technological applications. Many possible devices have been theorized for example are spin field-effect transistors (spin-FET)[1] and storage devices which utilize spin-current and associated spin-transfer torque to efficiently manipulate magnetic domains [7, 6]. In spite of fundamental interest and potential for applications, the actual realization of these devices has been rather elusive. One of the main culprits for the limited success to date is that the devices require very granular, ideally electric, control of the spin, which is impeded by widely separated energy scales and weak coupling between magnetic and charge degrees of freedom. One class of materials that allow for such electric control of spin-polarized states are the ferroelectric semiconductors with large atomic spin-orbit coupling (SOC) [2, 5, 8]. Inversion symmetry breaking together with SOC results in a linear splitting of spin-polarized bands, seen in the band structure as a conical intersection surrounding a high-symmetry point of the Brillouin Zone (see Fig. 4.1). Thus, current carriers (holes in the case of Fig. 4.1) travelling through the material will tend to align their spins to these spin-polarized bands. As we discuss in more detail in the following, the direction of the spin polarization depends on the orientation and strength of the electric field \mathbf{E} . In ferroelectrics, an internal field results from the polarization P , allowing it to be tuned and switched by an external applied electric field. These spin-polarized states have been observed both experimentally [5, 10, 9], and from *ab-initio* density functional theory (DFT) simulations [2]. It is, however, often not well understood and often misattributed what the underlying microscopic mechanisms are that lead to the observed splitting. [explicit mentions? Maybe too aggressive]

We investigate multiple different origins of this k and E dependent spin-

splitting. The discussed contributions arise due to the Hamiltonian of form

$$H_R(\mathbf{k}) = \alpha_R \frac{\mathbf{E}}{|\mathbf{E}|} \cdot (\mathbf{k} \times \hat{\sigma}), \quad (4.1)$$

where $\hat{\sigma}$ is the electron spin operator, and \mathbf{E} the electric field. It will turn out that multiple microscopic effects can lead to contributions of this form, some of these are well known, others are more obscure. The magnitude of the contribution depends on the microscopic origin, namely whether the effect is purely relativistic or rather a combination of relativistic and electrostatic. Certain materials showcase an exceedingly big splitting, for example in GeTe as can be seen in Fig. 4.1, and will be used as the main example throughout this chapter.

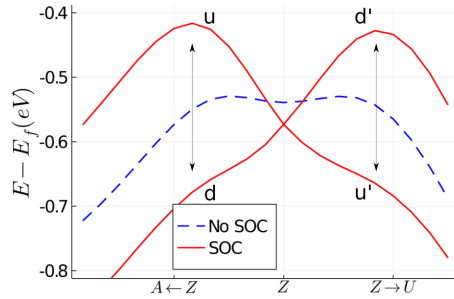


Figure 4.1: **Large Rashba splitting in GeTe** The two graphs show the band dispersions for the first valence band for the non spin-orbit coupled (NSOC, blue), and spin-orbit coupled (SOC, red) case, around the high-symmetry Z point of the Brillouin zone (see Fig. 4.4 for details). The $u - d$ and $u' - d'$ labels designate the up and down spin-polarized bands, where the prime signifies that the orientation of the spin axis depends on specific path followed in k -space.

We hope that this will shed light on where these contributions come from and how they compare with each other and how they ultimately lead to the observed spin-splitting.

4.2 Rashba-Bychkov Effect

The first discovered and most well known effect bearing the form of Eq. 4.1 is the Rashba-Bychkov effect, first derived in their seminal 1959 paper[15]. It is a relativistic effect that is derived from an expansion to second order in $1/c$, c denoting the speed of light, of the electronic Dirac equation (where the Fouldy-Wouthuysen transformation was applied):

$$\mathcal{H}\psi = \left[\frac{\mathbf{p}^2}{2m} - eV - \frac{e\hbar}{4m^2c^2} (\boldsymbol{\sigma} \cdot [\nabla V \times \mathbf{p}]) - \frac{\hbar^2}{8m^2c^2} \Delta V - \frac{\mathbf{p}^4}{8m^3c^2} \right] \psi = E\psi \quad (4.2)$$

where ψ is a two component spinor, V denotes the electric potential, $\boldsymbol{\sigma}$ a vector of Pauli-matrices ($\sigma_x, \sigma_y, \sigma_z$), m and e the electron mass and charge respectively, and \mathbf{p} the canonical momentum. The first two terms are the nonrelativistic part

of the Hamiltonian, the third represents the SOC, the fourth is known as the Darwin effect and the fifth is the relativistic correction to the effective electron mass. As is common in literature, we introduce the spin-orbit coupling constant $\lambda = \frac{e\hbar}{4m^2c^2}$. In a crystal with a periodic potential $V(\mathbf{r})$, electronic wavefunctions are Bloch wavefunctions $\psi_n(\mathbf{k}, \mathbf{r}) = u_n(\mathbf{k}, \mathbf{r})e^{i\mathbf{k}\cdot\mathbf{r}}$, where u_n denotes the cell-periodic part, and n is the band index. To obtain the eigenvalue equation for $u_n(\mathbf{k}, \mathbf{r})$, we insert ψ_n in Eq. 4.2, and carry out the differentiation $\mathbf{p} e^{i\mathbf{k}\cdot\mathbf{r}} u_n(\mathbf{k}, \mathbf{r}) = e^{i\mathbf{k}\cdot\mathbf{r}} (\mathbf{p} + \mathbf{k}) u_n(\mathbf{k}, \mathbf{r})$, and similarly $\mathbf{p}^2 \rightarrow (\mathbf{p} + \mathbf{k})^2$. This leads to the following equation for $u_n(\mathbf{k}, \mathbf{r})$:

$$E_n u_n(\mathbf{k}, \mathbf{r}) = (V_0 + V_1 + V_2 + V_3) u_n(\mathbf{k}, \mathbf{r}) \quad (4.3)$$

$$V_0(\mathbf{k}) = \frac{\mathbf{p}^2}{2m} - eV + \frac{\hbar^2 k^2}{2m} \quad (4.4)$$

$$V_1(\mathbf{k}) = \hbar \frac{\mathbf{k} \cdot \mathbf{p}}{m} \quad (4.5)$$

$$V_2(\mathbf{k}) = -\lambda \boldsymbol{\sigma} \cdot (\nabla V \times \mathbf{k}) \quad (4.6)$$

$$V_3(\mathbf{k}) = -\lambda \boldsymbol{\sigma} \cdot (\nabla V \times \mathbf{p}). \quad (4.7)$$

We neglected the last two terms of Eq. 4.2 since they are exceedingly small and don't contribute to the linear form of Eq. 4.1. It is important to understand how the electric fields inside the crystal contribute to V_2 and V_3 , where both terms originate from the application of \mathbf{p} to either $u_n(\mathbf{k}, \mathbf{r})$ or $e^{i\mathbf{k}\cdot\mathbf{r}}$, respectively. We first separate ∇V in two contributions, one coming from the potential wells created by the atoms, and another originating from the ferroelectric polarization (it is assumed that no external fields are applied):

$$\nabla V = \mathbf{E} = \mathbf{E}_{at} + \mathbf{E}_P \quad (4.8)$$

These contributions, together with the two parts of the Bloch functions (i.e. the cell periodic $u_n(\mathbf{k}, \mathbf{r})$, and envelope function $e^{i\mathbf{k}\cdot\mathbf{r}}$) are pictorially shown in Fig. 4.2.

Looking at the picture, it becomes clear that the contribution of the atomic potential applied to the envelope function is zero because while k is a constant, E_{at} is odd throughout the unit cell, leading to the contributions on either side of the potential well to cancel out. Thus the only contribution to the first term in Eq. 4.9 comes from the uniform (even) E_P , which in general is very small compared to the atomic one. A similar argument can be applied to the contribution to V_3 . Due to the shape of the periodic part of the wavefunction, only the contribution coming from E_{at} will be nonzero, this is essentially the well-known atomic spin-orbit coupling and can be rather large.

In the following it is assumed that Eq. 4.3 can be solved for a time reversal (TR) invariant point \mathbf{k}_0 in the first BZ, where the two spin states are necessarily degenerate. Due to the broken inversion symmetry and inclusion of the SOC terms (V_2, V_3), this degeneracy will be broken for k points away from the TR invariant point. We denote the two degenerate states at \mathbf{k}_0 by $|u_n^\downarrow\rangle$ and $|u_n^\uparrow\rangle$. It is important to realize that the orientation of spin axis of the eigenstates of Eq. 4.3 depends on the direction of both \mathbf{k} and \mathbf{P} , as will become clear later. Without loss of generality we take $\mathbf{k}_0 = \mathbf{0}$ and $E_n^{\uparrow, \downarrow}(\mathbf{0}) = 0$. Expanding in the deviation away from the high-symmetry point, in the usual $\mathbf{k} \cdot \mathbf{p}$ sense, and

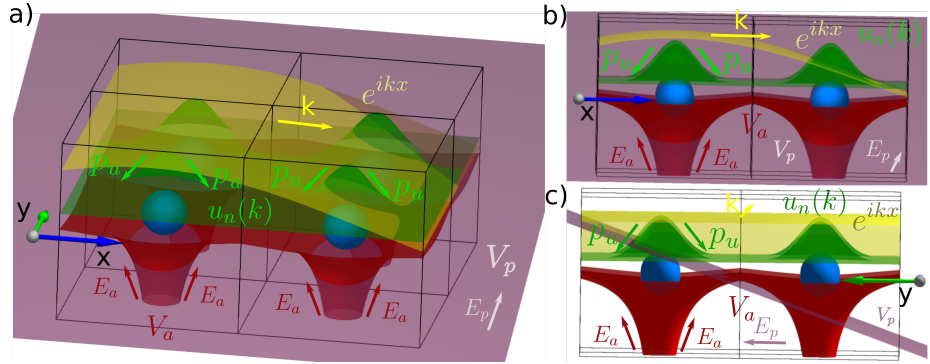


Figure 4.2: Pictorial representation of the different electric potentials (V) and fields (E) in a 2D square lattice. The blue spheres show the atoms, which produce the spherically symmetric red potential V_a and field E_a . The purple slab denotes a uniform ferroelectric polarization potential V_p which in this case is directed along the crystalline y -direction, creating field E_p . The green and yellow surfaces denote two components of the Bloch function: $u_n(k)e^{ikx}$, where the yellow is the envelope plane wave part and the green the cell periodic part.

keeping only linear \mathbf{k} terms and terms up to second order in $1/c$, we get

$$E_n^{\sigma_1}(\mathbf{k}) = -V_2^{\sigma_1}(\mathbf{k}) + \quad (4.9)$$

$$\sum_{m,\sigma_2=\uparrow,\downarrow} \frac{\langle u_n^{\sigma_1} | V_1(\mathbf{k}) | u_m^{\sigma_2} \rangle \langle u_m^{\sigma_2} | V_3(\mathbf{k}) | u_n^{\sigma_1} \rangle + h.c.}{E_n^{\sigma_1} - E_m^{\sigma_2}}, \quad (4.10)$$

where the sum over m, σ_2 includes all states which are not equal to n, σ_1 .

Even though the latter term of Eq. 4.9 is of higher order in the perturbation theory, it usually has the same order of magnitude as the former. This can be understood from the previous discussion on the origin of various terms in Eq. 4.3, and in particular what fields contribute to V_2 or V_3 . For this to be true, however, it is important that the orbitals u_n , and u_m in the second term have contributions that originate from an atom with a strong spin-orbit coupling. From the point of view of symmetries, another requirement for the second term to be nonzero is that u_n and u_m have contributions that have different parity, since \mathbf{p} is odd in spatial coordinates, $\mathbf{k} \cdot \mathbf{p}$ is only non-zero when one of the orbitals is odd with respect to a spatial direction and the other even. One example could be a p_y orbital and a $s-p_z$ hybridized one, which would be created by the ferroelectricity with electric polarization along the z -axis (add drawing? add hopping matrix?).

4.3 Orbital Rashba Effect

Unlike the purely relativistic Rashba-Bychkov effect, the orbital effect combines strong atomic SOC with the generation of nonzero orbital angular momentum (OAM) through electrostatic means. This contribution, therefore, is not limited by the small prefactors of Eq. 4.9. As will be explicitly shown below, electric dipole matrix element s can cause Bloch functions to acquire nonzero OAM

when any electric field is present (e.g. from electric polarization), and vice versa Bloch functions with nonzero OAM acquire nonzero electric dipoles between unit cells[13, 12, 4]. This leads to two separate effects.

Firstly, when atomic SOC is included, OAM is unquenched at the high symmetry k-points. This leads to a correction to the band dispersion that varies linearly with \mathbf{k} . Secondly, even without including the contribution of the atomic SOC, the OAM of the Bloch functions to appear in a chiral texture as one moves away from the high-symmetry k-point, similarly to how the relativistic Rashba effect leads to a chiral spin texture. If one then includes the atomic SOC from Eq. 4.3, this linear-in-k l will lead to a linear variation of the energy with either positive or negative slope, depending on the spin orientation.

We now proceed by giving a pedagogical derivation of this mechanism based on a tight-binding model [13, 4].

4.3.1 Tight-Binding model

The tight-binding model is defined on a 2D square layer with one atom per unit cell, and four Wannier orbitals on the atom. We assume that these orbitals are gaussians the form $s(\mathbf{r}, \mathbf{n}) = e^{-\frac{|\mathbf{r}-\mathbf{n}|^2}{a_0}}$, $p_\alpha(\mathbf{r}, \mathbf{n}) = \alpha e^{-\frac{|\mathbf{r}-\mathbf{n}|^2}{a_0}}$ with $\alpha = x, y, z$, and \mathbf{n} denoting the unit cell indices $\mathbf{n} = (n_x, n_y)$. The reason for choosing gaussians is to make solving the overlap integrals more easy, it does not lead to any qualitative changes to the derivation below. To simplify notation below, we omit \mathbf{r} and write $|\alpha^0\rangle = |\alpha\rangle$. The bare tight-binding Hamiltonian is denoted as \hat{H}_0 and includes the usual hopping parameters due to overlap $t_{\alpha\beta}^{ij} = \int d\mathbf{r} w_i^\alpha(\mathbf{r})^* (\frac{\mathbf{P}^2}{2m} + V(\mathbf{r})) w_j^\beta(\mathbf{r})$. To mimick the inversion symmetry breaking in ferroelectric materials (i.e. with a polar space group), an electric field perpendicular to the layer (z direction) is applied. This allows extra hopping terms associated with $\hat{H}_{isb} = e(\hat{\mathbf{d}} \cdot \mathbf{E})$, with $\hat{\mathbf{d}}$ the electric dipole moment:

$$\langle s | \hat{H}_{isb} | p_z \rangle = 2eE_z \theta_z^n \quad (4.11)$$

$$\langle p_z | \hat{H}_{isb} | p_x(\mathbf{n}) \rangle = eE_z \theta_z^n n_x \quad (4.12)$$

$$\langle p_z | \hat{H}_{isb} | p_y(\mathbf{n}) \rangle = eE_z \theta_z^n n_y \quad (4.13)$$

with $\theta_z^n = -ae^{-\frac{1}{2}\left(\frac{a|\mathbf{n}|}{a_0}\right)^2} \frac{\pi^{\frac{3}{2}}}{16\sqrt{2}}$, other terms of \hat{H}_{isb} are zero. Fig. 4.3 shows pictorially how these terms arise from the electric dipoles between the shifted orbitals.

Solving the tight binding model for $k = 0$, one can treat \hat{H}_{isb} as a perturbation on \hat{H}_0 due to the smallness of E_z , leading to a hybridization between the s and p_z orbitals:

$$|\tilde{p}_z\rangle = |p_z\rangle + \frac{\langle s | 2eE_z \theta_z^n | p_z \rangle}{\varepsilon_z - \varepsilon_s} |s\rangle \quad (4.14)$$

$$|\tilde{s}\rangle = |s\rangle + \frac{\langle p_z | 2eE_z \theta_z^n | s \rangle}{\varepsilon_s - \varepsilon_z} |p_z\rangle, \quad (4.15)$$

where $\varepsilon_s = \langle s | \hat{H}_0 | s \rangle$ and $\varepsilon_z = \langle p_z | \hat{H}_0 | p_z \rangle$. In order to proceed, we only treat the important kinetic energy part of \hat{H}_0 and rewrite it in terms of this hybrid

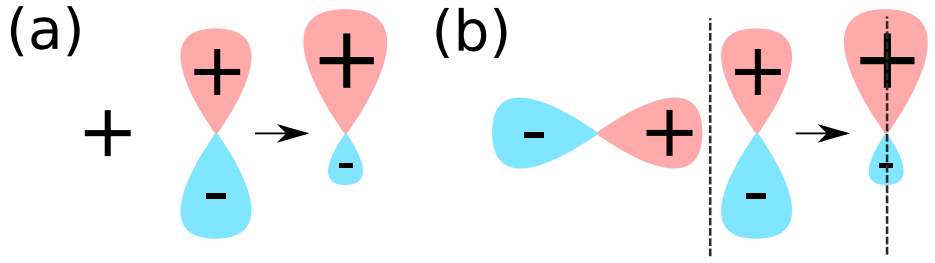


Figure 4.3: Overlap dipoles. (a) Dipole between s and p_z , (b) Dipole between shifted p orbitals, the dashed line signifies a unit cell boundary.

\tilde{p}_z orbital in the central unit cell and the shifted p_x, p_y orbitals, leading to:

$$\langle \tilde{p}_z | \hat{H}_0 | p_x(\mathbf{n}) \rangle = \frac{2eE_z\theta_z^n}{\varepsilon_z - \varepsilon_s} \langle s | \frac{-\nabla^2}{2} | p_x(\mathbf{n}) \rangle \quad (4.16)$$

$$= \frac{4eE_z(\theta_z^n)^2}{\varepsilon_z - \varepsilon_s} n_x (-5 + a^2|\mathbf{n}|^2) \quad (4.17)$$

$$\langle \tilde{p}_z | \hat{H}_0 | p_y(\mathbf{n}) \rangle = \frac{4eE_z(\theta_z^n)^2}{\varepsilon_z - \varepsilon_s} n_y (-5 + a^2|\mathbf{n}|^2) \quad (4.18)$$

To construct $\hat{H}_0(\mathbf{k})$ and $\hat{H}_{isb}(\mathbf{k})$, one can fourier transform the Wannier Functions:

$$|\alpha(\mathbf{k})\rangle = \frac{1}{\sqrt{N}} \sum_{\mathbf{n}} e^{i\mathbf{k}\cdot\mathbf{n}} |\alpha(\mathbf{n})\rangle \quad (4.19)$$

i with α one of the aforementioned orbitals, \mathbf{k} written in terms of crystalline coordinates ($\frac{2\pi}{a}$), and N denoting the total amount of unit cells in the material. This results in:

$$\hat{H}_0(\mathbf{k}) + \hat{H}_{isb}(\mathbf{k}) = \sum_{\mathbf{n}} e^{i\mathbf{k}\cdot\mathbf{n}} (\hat{H}_0(\mathbf{n}) + \hat{H}_{isb}(\mathbf{n})) \quad (4.20)$$

$$= \sum_{\mathbf{n}} i \sin(\mathbf{k} \cdot \mathbf{n}) (\hat{H}_0(\mathbf{n}) + \hat{H}_{isb}(\mathbf{n})) + k\text{-even terms}, \quad (4.21)$$

keeping only the $\sin(\mathbf{k} \cdot \mathbf{n})$ part of the exponent since the $\cos(\mathbf{k} \cdot \mathbf{n})$ part does not result in linear-in- k terms, in the small \mathbf{k} expansion below we keep only these linear-in- k terms.

If we then assume that at $k = 0$ the Bloch functions are formed from p_x, p_y, \tilde{p}_z and \tilde{s} orbitals: $|\alpha(\mathbf{k} = \mathbf{0})\rangle = \frac{1}{\sqrt{N}} \sum_{\mathbf{n}} |\alpha(\mathbf{n})\rangle$ a perturbation theory for small deviations \mathbf{k} away from zero can be written down:

$$|\alpha(\mathbf{k})\rangle = |\alpha\rangle + \sum_{\beta \neq \alpha} \frac{\langle \beta | \hat{H}_0(\mathbf{k}) + \hat{H}_{isb}(\mathbf{k}) | \alpha \rangle}{\varepsilon_{\alpha} - \varepsilon_{\beta}} |\beta\rangle \quad (4.22)$$

Gathering the linear-in- k terms, and assuming $\varepsilon_p = \langle p_x | \hat{H}_0 | p_x \rangle = \langle p_y | \hat{H}_0 | p_y \rangle$,

we find

$$|\tilde{p}_x(\mathbf{k})\rangle = |p_x(0)\rangle + \Theta \frac{ieE_z k_x}{\varepsilon_p - \varepsilon_{\tilde{z}}} |\tilde{p}_z(0)\rangle \quad (4.23)$$

$$|\tilde{p}_y(\mathbf{k})\rangle = |p_y(0)\rangle + \Theta \frac{ieE_z k_y}{\varepsilon_p - \varepsilon_{\tilde{z}}} |\tilde{p}_z(0)\rangle \quad (4.24)$$

$$|\tilde{p}_z(\mathbf{k})\rangle = |\tilde{p}_z(0)\rangle + \Theta \frac{ieE_z}{\varepsilon_p - \varepsilon_{\tilde{z}}} (k_x |p_x(0)\rangle + k_y |p_y(0)\rangle), \quad (4.25)$$

with $\Theta = \frac{\pi^{5/2}}{256a^3} \left(-16\sqrt{2} + \frac{3a\pi^{3/2}}{\varepsilon_z - \varepsilon_s} \right)$. Then, using the definition of the OAM operators for p -orbitals:

$$\hat{L}_x = \begin{pmatrix} 0 & 0 & 0 \\ 0 & 0 & -i \\ 0 & i & 0 \end{pmatrix}, \hat{L}_y = \begin{pmatrix} 0 & 0 & i \\ 0 & 0 & 0 \\ -i & 0 & 0 \end{pmatrix}, \hat{L}_z = \begin{pmatrix} 0 & -i & 0 \\ i & 0 & 0 \\ 0 & 0 & 0 \end{pmatrix} \quad (4.26)$$

we find that,

$$\langle \tilde{p}_z(\mathbf{k}) | \hat{L}_x | \tilde{p}_z(\mathbf{k}) \rangle = -2\Theta \frac{eE_z k_y}{\varepsilon_p - \varepsilon_{\tilde{z}}} \quad (4.27)$$

$$\langle \tilde{p}_z(\mathbf{k}) | \hat{L}_y | \tilde{p}_z(\mathbf{k}) \rangle = 2\Theta \frac{eE_z k_x}{\varepsilon_p - \varepsilon_{\tilde{z}}} \quad (4.28)$$

These expressions for \hat{L} can be filled into the expression for the atomic SOC $\hat{H}_{soc} = \lambda \hat{\mathbf{L}} \cdot \hat{\boldsymbol{\sigma}}$ to find the energy for $|\tilde{p}_z\rangle$:

$$\varepsilon(\mathbf{k}) = \frac{2\lambda\Theta e E_z}{\varepsilon_p - \varepsilon_{\tilde{z}}} (\mathbf{k} \times \boldsymbol{\sigma}) \quad (4.29)$$

which has the form of Eq. 4.1.

From this qualitative derivation, it is clear that the main reason behind the orbital Rashba effect can be traced back to the observation that Bloch functions with nonzero OAM have electric dipoles that couple to the inversion symmetry breaking electric field. We identified two sources that lead to the effect: the first one comes from the direct overlap dipoles between p_x and p_y orbitals, and the p_z orbital[13], the second is due to the hybridization of the s and p_z overlap, and the kinetic energy term between the s and neighboring p_x and p_y orbitals[4]. These two terms are reflected in the two terms that contribute to Θ , and lead to a chiral, linear-in- k texture of the OAM. If there then exists strong atomic SOC, this linear-in- k OAM will couple to the spin and result in the final Rashba-like form of Eq. 4.29.

There is one final term that contributes to the linear variation of OAM with \mathbf{k} , which is only present when there is an unquenching of the OAM at the high symmetry point ($|k| = 0$) due to the atomic SOC ???. This is due to the energy gain from \hat{H}_{soc} if the material has orbitals that have $\mathbf{j} = \mathbf{l} + \frac{1}{2}\boldsymbol{\sigma}$. Similar to the above derivation a small- k expansion for orbitals with nonzero OAM can be performed, leading in general to:

$$\langle \alpha | \hat{L}_\gamma | \beta \rangle = i\epsilon_{\alpha\beta\gamma} c_\alpha^* c_\beta \quad (4.30)$$

when α, β, γ designate x, y, z . This means that there has to be at least some admixing of multiple p -orbitals to get nonzero OAM. This leads to the following expansion of the Bloch functions around the high-symmetry $|k| = 0$ point:

$$|\psi(\mathbf{k})\rangle = \sum_{\mathbf{n}, \alpha} c_\alpha(\mathbf{k}) e^{i\mathbf{k}\cdot\mathbf{n}} |\alpha(\mathbf{n})\rangle \quad (4.31)$$

$$= \sum_{\mathbf{n}, \alpha} \left(c_\alpha(0) + \mathbf{k} \frac{\partial c_\alpha(\mathbf{k})}{\partial k} \Big|_{\mathbf{k}=0} \right) (1 + i\mathbf{k}\cdot\mathbf{n}) |\alpha(\mathbf{n})\rangle. \quad (4.32)$$

Focusing on the terms that vary linearly with k , the second term in the c expansion together with the first term in the exponent expansion is exactly the contribution that was discussed before. The final term for the Orbital Rashba effect originates from combining the first term in the c expansion with the second in the exponent expansion, leading to the contribution

$$\varepsilon(\mathbf{k}) = \langle \psi(\mathbf{k}) | \hat{H}_{isb} | \psi(\mathbf{k}) \rangle = i \sum_{\mathbf{n}, \alpha, \beta} c_\alpha^*(0) c_\beta(0) \mathbf{k} \cdot \mathbf{n} \langle \alpha(0) | \hat{H}_{isb} | \beta(\mathbf{n}) \rangle \quad (4.33)$$

$$= ieE_z \frac{-\pi^{5/2}}{8\sqrt{2}a^3} (c_x^*(0)c_z(0)k_x + c_y^*(0)c_z(0)k_y) \quad (4.34)$$

$$= eE_z \frac{\pi^{5/2}}{8\sqrt{2}a^3} (L_y(0)k_x - L_x(0)k_y). \quad (4.35)$$

These expressions show us that, due to $\hat{H}_{soc} = \lambda \hat{\mathbf{L}} \cdot \hat{\boldsymbol{\sigma}}$ and $\hat{H}_{isb} = eE_z d_z$, an additional Rashba-like term appears in the energy dispersion.

With the understanding that one can find Rashba like dispersions, coming not from the usually considered purely relativistic, but also from electrostatic mechanisms. We now look at a concrete example that behaves very similar to the above toy model, GeTe.

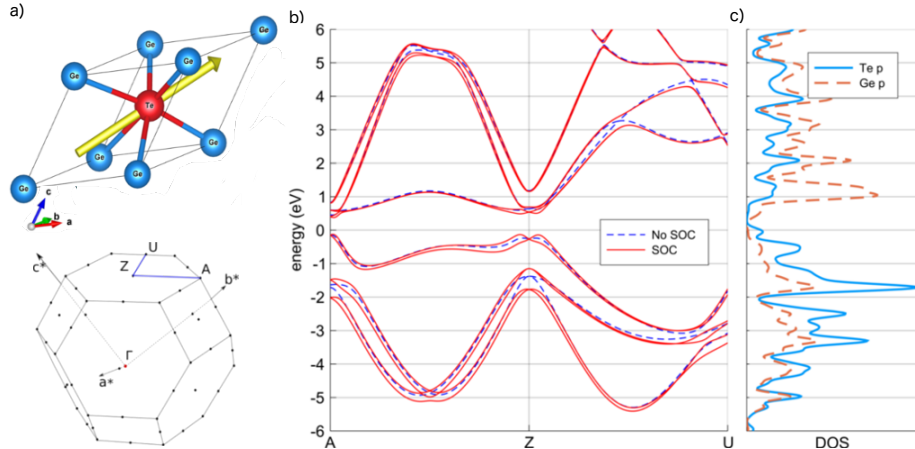


Figure 4.4: (a) Rhombohedral unit cell and Brillouin zone of GeTe, with the polarization direction in yellow. (b) Band structure obtained from a DFT calculation with and without SOC, along the blue path in panel (a). (c) partial DOS for Te and Ge p orbitals computed without SOC.

4.4 Overview: Germanium Telluride

The space group of GeTe is $R\bar{3}m$ (#160 in International Tables), with ferroelectric polarization along the threefold rotation z -axis caused by an off-centering of the central Te atom [14] as displayed in Fig. 4.4-(a). The valence and conduction bands are formed mostly by s and p orbitals from Te and Ge, respectively. This, together with the large spin-splitting in the vicinity of the Z point [2] as observed from the bandstructure in Fig. 4.4-(b), lends it as a perfect test-case for the above described mechanisms. Moreover, since it is a bulk material, the relativistic Rashba effects contribute negligibly due to the small potential gradients caused by bulk ferroelectricity. The band structure, presents a distinct large linear spin splitting around the Z point, along the $Z - A$ and $Z - U$ paths. The $Z - \Gamma$ path shows no splitting because the electric field is along the z direction, and as shown by the above derivation, only k_x and k_y will show a linear splitting. The density of states (DOS), displayed in Fig. 4.4-(c), confirms the orbital character of the bands.

4.5 Methods

We performed ab-initio DFT calculations using the Quantum-Espresso software package[3]. In order to confirm the linear varying OAM even when spin-orbit is not included we performed non-relativistic, as well as relativistic calculations. Both were performed using ONCVPSP pseudopotentials, with 30 Ry for the energy cutoff, and 160 Ry for the density cutoff. The reciprocal space was sampled using a 10x10x10 and 6x6x6 Monkhorst-Pack grid for the self-consistent and non-self-consistent calculations, respectively, using an energy convergence threshold of 10^{-7} Ry. Afterwards we used the Wannier90 package [11] to perform the Wannierization, using atomic s and p -orbitals on both Ge and Te. This provides us with the tools to analyze the real space properties of Bloch functions such as the dipole moment and OAM.

4.6 Band structure

The bands we will focus on most are the three topmost valence bands. As seen in Fig. 4.4-(b), these bands have the largest spin-splitting. This suggests that indeed the atomic SOC plays an important role, seen as these bands are comprised mostly of Te orbitals, and SOC is largest on Te. If one were to fit the dispersion of the topmost band to Eq. 4.1, it results in a large prefactor $\alpha_R \approx 30.7 \text{ eV}\cdot\text{\AA}$ [2]. As discussed before, a more realistic prefactor would be $\alpha_R = 10^{-6} \text{ eV}$ in the purely relativistic case inside the vacuum.

The last issue with the purely relativistic explanation, which has been confirmed experimentally[9], lies in the orientation of the spin polarization of the split bands. According to Eq. 4.1, the bands should all be split equally and Bloch functions at the same k -point should have the same spin orientations, since their character does not enter Eq. 4.1. However, as has been shown and will be confirmed by our results below, the orientation depends on the character of the band, more specifically on the value of the total angular momentum j .

4.7 Results and Discussion

The dispersion, OAM, and SAM of the first valence band are shown in the left panel of Fig. 4.6. Confirming our earlier conclusions, we can see that non-zero, linearly varying OAM is formed as we move away from the high-symmetry Z -point. Moreover, the OAM is perpendicular to both the z -axis and the k vector, as it should be from Eq. 4.27, and can also be seen from the panels in Fig. 4.8. This leads e.g. to $l_y = 0$ along the $A \rightarrow Z$ path, where only k_y is nonzero. When atomic SOC is included in the orange and blue graphs, we see the spin-splitting that results from having the spin oriented either along or opposite to the already linearly varying OAM. The unquenching of the OAM at the Z -point when SOC is included is also clearly visible, together with the resulting change in the slope that originates from the corresponding contribution to the dipole moment Eq. 4.33. This correlation can also be observed in the panel showing the center of mass $\bar{z} = \int_{\text{supercell}} z|\psi(k)|^2$ of the Bloch-functions, which is proportional to the dipole moment around the same reference point.

When we compare this first valence band with the third valence band, shown in the right panel of Fig. 4.6, we can clearly see the previously discussed issues with the purely relativistic explanation. As stated before, we can note that not only the magnitude but also the sign of the prefactor in Eq. 4.1 is opposite for these two bands, showcased by the size of the splitting, and by the ordering of the spin-up vs the spin-down splitted part. This is because the character of the first and third valence bands are different. The first valence band is mostly coming from Te $j = \frac{3}{2}$ orbitals, whereas the third valence band is predominantly $j = \frac{1}{2}$. This causes the orientation of the OAM and SAM to be along each other in the first band, and opposite for the third, as shown in Fig. 4.8. This then leads to the different ordering of the spin-split bands.

There is one last very interesting feature one can notice from Fig. 4.8 (c) and (f), that is, the switching of the character (and SAM, OAM orientation) of the bands, very close to the Z point. This is because the crystal field breaks rotational symmetry causing the atomic j to not be a conserved quantity, i.e.

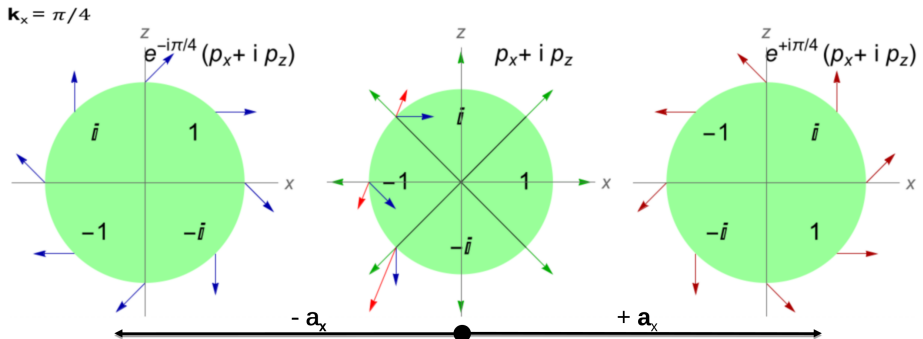


Figure 4.5: Interference between orbitals with nonzero OAM. Three neighboring unit cells are displayed, each with the same $p_x + ip_z$ orbital (thus having nonzero l_y). The wave functions of the left and right unit cells have their phase rotated by the plane-wave part $e^{ik_x R_x}$. The amplitude and phase of the wave function are encoded with the length and polar angle of the arrows.

there is a mixing between different atomic j orbitals, which varies strongly in this very narrow region around Z .

All these considerations lead to a very nontrivial SAM and OAM texture of the bands as we progress through the BZ.

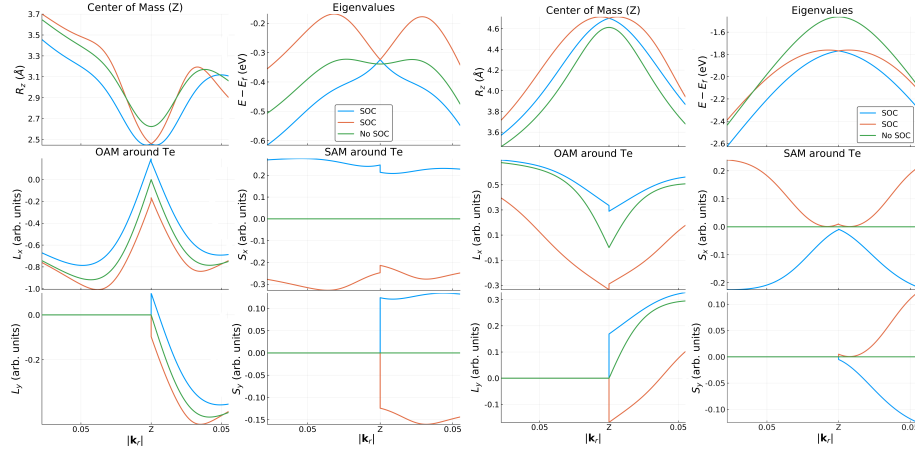


Figure 4.6: Comparison between the real-space observables and energy dispersion in (a) the first and (b) third valence band. The values are plotted in function of the relative distance from the Z point $\mathbf{k}_r = \mathbf{k} - \mathbf{k}_Z$, towards the A and U points. The green graphs denote the values before turning on atomic SOC, whereas the orange and blue graphs denote the two spin-split bands.

4.8 Conclusions

We have explored the microscopic origin of the giant Rashba-like spin splitting in the band structure of bulk ferroelectric GeTe with high atomic SOC. We derived the form of the band dispersion in the Wannier representation, that relates the large spin splitting to the intricate interplay between OAM, atomic SOC, the crystal field and the electric polarization. It turns out that the crucial component, which is not present in the relativistic Rashba effect, is the emergence of a nonzero electric dipole of the Bloch functions due to their OAM. The quantitative analysis based on Wannier functions and atomic-centered approximation confirms this mechanism in GeTe. We find a very good agreement between the proposed band dispersion, Eq. (??), and the dispersions of the first and third valence bands, where the effect manifests itself most clearly.

Ultimately, the results suggest that (1) large ferroelectric polarization, (2) high atomic SOC, and (3) highly symmetric environment producing little OAM quenching could be the design rules for new materials with strong Rashba-like spin splitting. These materials could enable spintronic devices with the much needed electric control of spin polarization.

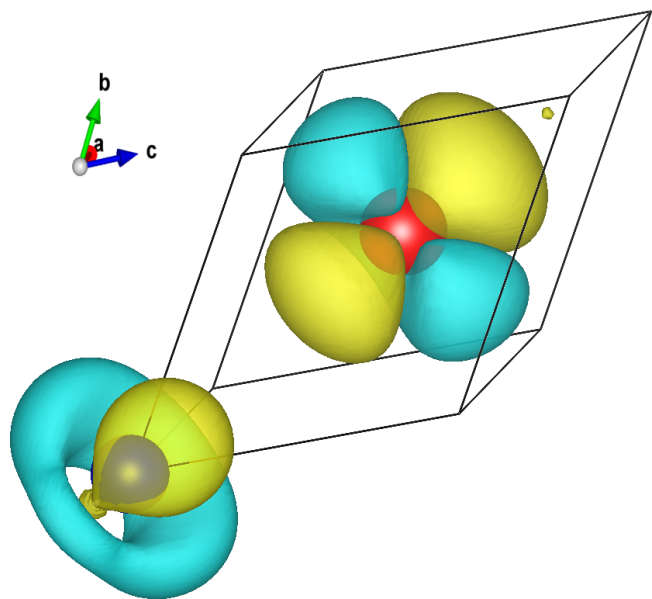


Figure 4.7: The variation of the charge density of the Bloch function of the first valence band $\frac{\partial|\psi(k)|^2}{\partial k}\Big|_{k=Z}$ away from Z towards A . Te and Ge ions are in red and blue, respectively. The charge asymmetry around Ge showcases the nonzero dipole moment along z , which couples to the local electric field near Ge ion.

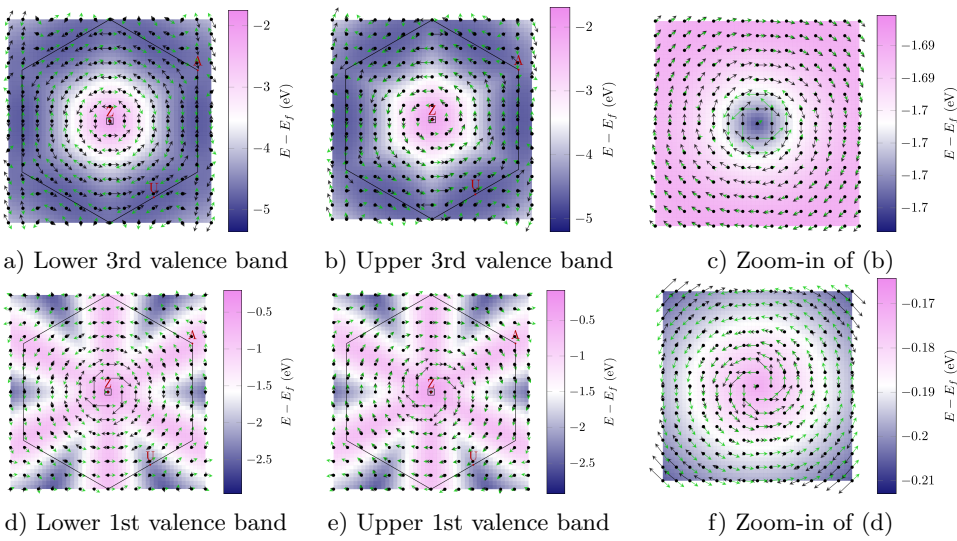


Figure 4.8: OAM and SAM textures around the Z point in the first and third valence bands of GeTe. The black and green arrows show the OAM and SAM textures, respectively. The length of the arrows was chosen separately for clarity in each figure and should thus not be compared. The color maps signify the energy of the bands, relative to the Fermi level. The small box around the Z point indicates the area, magnified in panels (c) and (f). In the zoomed figures (c) and (f) one can observe the change or relative orientation between the SAM and OAM when moving away from the Z point, signifying a change of character between $j = 1/2$ and $j = 3/2$.

Bibliography

- [1] Supriyo Datta and Biswajit Das. “Electronic analog of the electro-optic modulator”. In: *Applied Physics Letters* 56.7 (1990), pp. 665–667. ISSN: 00036951. DOI: 10.1063/1.102730.
- [2] Domenico Di Sante et al. “Electric control of the giant rashba effect in bulk gete”. In: *Advanced Materials* 25.4 (2013), pp. 509–513. ISSN: 09359648. DOI: 10.1002/adma.201203199.
- [3] Paolo Giannozzi et al. “QUANTUM ESPRESSO: a modular and open-source software project for quantum simulations of materials.” In: *Journal of physics. Condensed matter : an Institute of Physics journal* 21.39 (2009), p. 395502. ISSN: 0953-8984. DOI: 10.1088/0953-8984/21/39/395502.
- [4] Dongwook Go et al. “Surface orbitronics: new twists from orbital Rashba physics”. In: 1 (2016), pp. 1–8. ISSN: 2045-2322. DOI: 10.1038/srep46742. URL: <http://arxiv.org/abs/1611.04674> %0Ahttp://dx.doi.org/10.1038/srep46742.
- [5] K Ishizaka. “Giant Rashba-type spin splitting in bulk BiTeI”. In: *Nature materials* 10.7 (2011), pp. 521–526. ISSN: 1476-1122. DOI: 10.1038/nmat3051. URL: <http://dx.doi.org/10.1038/nmat3051>.
- [6] T Jungwirth et al. “Antiferromagnetic spintronics”. In: *Nature Nanotechnology* 11.3 (2016), pp. 231–241. ISSN: 1748-3387. DOI: 10.1038/nnano.2016.18. URL: <http://www.nature.com/doifinder/10.1038/nnano.2016.18>.
- [7] Andrew D. Kent and Daniel C. Worledge. “A new spin on magnetic memories”. In: *Nature Nanotechnology* 10.3 (2015), pp. 187–191. ISSN: 1748-3387. DOI: 10.1038/nnano.2015.24. URL: <http://www.nature.com/doifinder/10.1038/nnano.2015.24>.
- [8] Minsung Kim et al. “Switchable $S = 1/2$ and $J = 1/2$ Rashba bands in ferroelectric halide perovskites.” In: *Proceedings of the National Academy of Sciences of the United States of America* 111.19 (2014), pp. 6900–4. ISSN: 1091-6490. DOI: 10.1073/pnas.1405780111. URL: <http://www.pnas.org/cgi/content/long/111/19/6900>.
- [9] J. Krempaský et al. “Surface versus bulk contributions to the giant Rashba splitting in the ferroelectric $\{\alpha\}$ -GeTe(111) semiconductor”. In: 111 (2015), pp. 1–10. DOI: 10.1103/PhysRevB.94.205111. URL: <http://arxiv.org/abs/1503.05004> %0Ahttp://dx.doi.org/10.1103/PhysRevB.94.205111.

- [10] Marcus Liebmann et al. “Giant Rashba-Type Spin Splitting in Ferroelectric GeTe(111)”. In: *Advanced Materials* 28.3 (2016), pp. 560–565. ISSN: 15214095. DOI: 10.1002/adma.201503459.
- [11] Arash A. Mostofi et al. “An updated version of wannier90: A tool for obtaining maximally-localised Wannier functions”. In: *Computer Physics Communications* 185.8 (2014), pp. 2309–2310. ISSN: 00104655. DOI: 10.1016/j.cpc.2014.05.003.
- [12] Seung Ryong Park et al. “Orbital-angular-momentum based origin of rashba-type surface band splitting”. In: *Physical Review Letters* 107.15 (2011), pp. 1–5. ISSN: 00319007. DOI: 10.1103/PhysRevLett.107.156803.
- [13] L. Petersen and P. Hedegård. “Simple tight-binding model of spin-orbit splitting of sp-derived surface states”. In: *Surface Science* 459.1 (2000), pp. 49–56. ISSN: 00396028. DOI: 10.1016/S0039-6028(00)00441-6.
- [14] K. M. Rabe and J. D. Joannopoulos. “Theory of the structural phase transition of GeTe”. In: *Physical Review B* 36.12 (1987), pp. 6631–6639. ISSN: 01631829. DOI: 10.1103/PhysRevB.36.6631.
- [15] Emmanuel Rashba and V. Sheka. “Symmetry of Energy Bands in Crystals of Wurtzite Type II . Symmetry of Bands with Spin-Orbit Interaction”. In: *Fiz. Tverd. Tela: Collected Papers* 2 (1959), pp. 162–76.

Chapter 5

Coupling between spin and strain density waves

5.1 Introduction

Chromium is an itinerant antiferromagnetic metal. It is the hallmark example of a material where a SDW develops due to local repulsive interactions of the electron gas, combined with a nesting of the fermi surface.

5.2 Experimental methods

Before focusing on the theoretical description of the coupling between the SDW and CDW, we take a look at the experimental techniques and results that we are seeking to reproduce. Optical pulses were used to heat up the material, mostly absorbed by the SDW order through photoexcitation. An x-ray free-electron laser (XFEL) is then used to probe the bragg-peaks of the CDW and how they change in time. The need of the XFEL can be attributed to the very short timescales at which the observed behavior is exhibited by the material, with resolutions of a couple femtoseconds being made accessible. The scattering intensity of the bragg peak is directly proportional to the magnitude of the CDW, offering both phase and amplitude information of the oscillation that we study. It is important to realize that the SDW order is not directly accessible through these kinds of measurements, so we are effectively studying the effect of exciting one order parameter through the reaction of the other due to the coupling between them. XFELs also allow for higher peak selectivity (narrow and intense satellite Bragg peaks), such that it allows for measurements performed on thin films even deposited on thick substrates, as was the case in the experiments performed by A. Singer et.al. The thin films offer a clarity in terms of describing the physics of this process, since it leads to a very even excitation of the entire volume, and it causes the order parameters to be homogeneous throughout the material. This absence of topological defects is confirmed by the absence of a widening of the satellite peak associated with the PLD, as compared with the peaks of the material itself. [not sure about this, I actually don't understand what they are talking about in the paper either]. To this end,

a 30nm thick Cr film was used in the experiments, harboring seven periods of the SDW perpendicular to the plane. This thinness of the film also decreases the Neel temperature to 290K, from the bulk value of around 307K. The pulses used to excite the SDW were 40 fs long, with a total intensity of 2.9 mJ/cm^2 . In the experiments with two sequential pulses the power of the second pulse was roughly half that of the first.

5.3 Theory

[some explanation of Peierls instabilities etc, the things that cause the SDW in the first place?]

To understand how modulation of bond lengths changes the magnetic exchange between spins of the constituent ions, it is instructive to recall where the Heisenberg exchange form comes from, namely the Hubbard model:

$$H = \sum_{\langle i,j \rangle} t_{ij} c_{i,\sigma}^\dagger c_{j,\sigma} + U \sum_i U n_i^\uparrow n_i^\downarrow \quad (5.1)$$

where $\langle i,j \rangle$ denotes nearest neighbors, and t_{ij} the hopping between them, and U_i the on-site coulomb repulsion active when the on-site orbital is occupied by more than one electron. In the usual case, $U \gg t_{ij}$ and thus a Shrieffer-Wolf transformation can be performed to separate the high energy from the low energy subspace. This amounts to performing a second order perturbation theory, allowing the Hubbard model to effectively be rewritten in terms of the on-site spins, leading to the well-known Heisenberg model:

$$H = \sum_{\langle i,j \rangle} J_{ij} \mathbf{S}_i \cdot \mathbf{S}_j, \quad (5.2)$$

with the coupling constant (often referred to as the magnetic exchange) $J_{ij} = t_{ij}^2/U$. Since hopping parameters are a result of the overlap between orbitals on neighboring sites, it is clear that they depend on the length of the bond r between them, i.e. $t_{ij} \sim r$ to first order. In materials where SDW are formed, this magnetostriction will lead to PLD leading to strain waves.

The geometry that is used in the experiment is such that a microscopic model as described above is unnecessary to describe the essential physics, since the Cr thin film can be considered to be homogeneous throughout the experiment. This allows us to instead adopt a continuum description utilizing a standard Landau theory with two order parameters describing the SDW (L) and PLD (y) and a coupling between them to describe the magnetostriction.

$$F = \frac{\alpha}{2}(T_L - T_c)L^2 + \frac{\beta}{4}L^4 - gL^2y + \frac{\omega_0}{2}y^2 + \frac{b}{4}y^4. \quad (5.3)$$

The double well potential that leads to the SDW is characterised by α and β , with the temperature of the SDW given by T_L , with the critical temperature T_c below which the phase transition occurs and the SDW order sets in. The coupling between the two order parameters is given by term with γ . Only even orders of L appear in the energy, since the energy is time reversal even, but L is time reversal odd. Notice, also, that the PLD order parameter y by itself would have a zero equilibrium value, the fourth order term with strength b is only

included to provide a better fit to some anisotropic features of the experiment, not to bound the energy as is required if y would also undergo a second order phase transition as L . The equilibrium value of y will, however, be shifted away from zero due to the force applied to it by the nonzero equilibrium value of L , a key feature of this model to bear in mind for later. y is thus a pure slave order parameter.

The temperature of the SDW T_L is described by a two temperature model, including a time-dependent heat source describing the XFEL pulses, and a bath with non infinite mass and temperature T_b , meaning that the bath temperature will increase.

$$c_L \dot{T}_L = -k(T_L - T_b) + q(t) \quad (5.4)$$

$$c_b \dot{T}_b = -k(T_b - T_L) \quad (5.5)$$

where c_L, c_b are the heat capacities of the SDW and the bath, k the heat transfer rate, and $q(t)$ signifies the heat injected into the system through the photon pulses, and is modeled by a gaussian $q(t) = \frac{f}{\tau\sqrt{\pi}}e^{-(t-t_0)^2/2\tau^2}$, where τ denotes the pulse width. The dots signify time derivatives.

In order to solve the time evolution of the system we start by incorporating the free energy given by Eq. 5.3 into the full Lagrangian

$$\mathcal{L} = \frac{m_L(\dot{L} + \gamma_L L)^2}{2} + \frac{m_y(\dot{y} + \gamma_y y)^2}{2} - F, \quad (5.6)$$

where the γ denote the damping parameters for both order parameters. This then leads to the well-known Euler-Lagrange equations given by

$$m_L \ddot{L} = -\alpha(T - T_c)L - \beta L^3 + 2gL y - \gamma_L \dot{L} \quad (5.7)$$

$$m_y \ddot{y} = gL^2 - \omega_0^2 y - b y^3 - \gamma_y \dot{y} \quad (5.8)$$

which we then solve numerically to get the time evolution of both order parameters.

5.4 Results

The experimental results we use as a basis to fit our model to are shown in Fig. 5.1. In the numerical model, we found in earlier trials that the dynamics of the SDW order parameter L is orders of magnitude faster than the ones from the PLD y , as expected. This can also be seen from Fig. 5.3 since the energy potential is a lot flatter for y than for L , leading to a slower time evolution. This difference in dynamics makes it extremely hard to solve the differential equations numerically, we therefore assumed that at each timestep the L order parameter is in equilibrium in its instantaneous energy potential. This is equivalent to the limit of the mass m_L in Eq. 5.7 going to zero. The value of L at a given T_L and y can be found by minimizing the Landau free energy 5.3 in terms of L such that $\frac{\partial F}{\partial L} = 0$, leading to:

$$L_0 = \pm \sqrt{\frac{\alpha(T_L - T_c) + 2gy}{\beta}}. \quad (5.9)$$

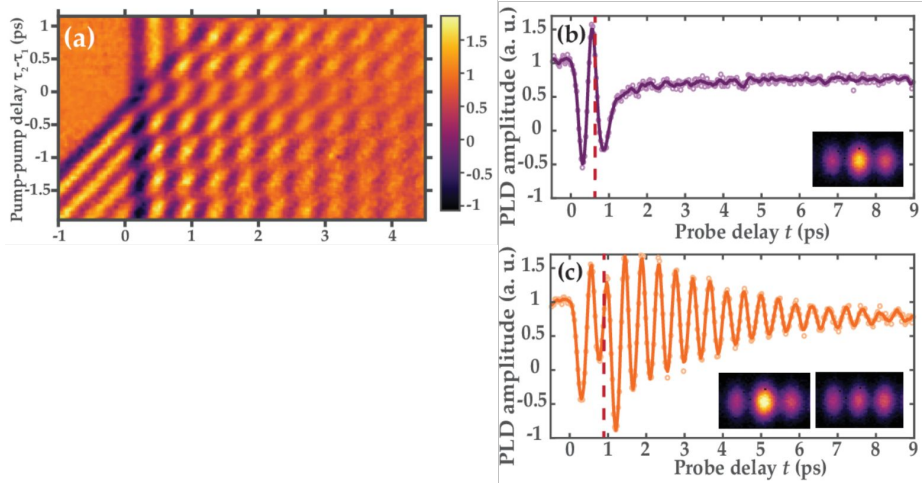


Figure 5.1: Experimental measurements. (a) Heatmap showing different pump-pump delay experiments. Notice the low intensity horizontal band around 0 ps pump-pump delay, where the oscillation amplitude is not at the maximum due to only one big pulse exciting the material and heating it through the phase transition, thus wasting a portion of the energy. The horizontal bands with alternating maximum and minimum magnitudes highlight constructive and destructive interference. (b-c), Magnitude of the strain wave in two extreme control cases, where (b) showcases maximum destructive interference, and (c) close to maximum constructive interference. Solid lines are experimental data (empty circles in figure) smoothed by a Savitzky-Golay filter. b – pump-pump delay of 620 fs, c – pump-pump delay of 845 fs.

This eliminates the need to evaluate Eq. 5.7, instead using Eq. 5.9 to evaluate L in the partial differential equation for the evolution of y .

We then took eleven representative experiments, which can be thought of as horizontal slices of Fig. 5.1(a), in order to fit the model parameters to get the best total fit across all datasets. The parameters are

$$\alpha = 6039, \beta = 7.97 \times 10^7, g = 0.52, \gamma_L = 25.0, \quad (5.10)$$

$$\omega_0 = 14.1, b = 3.38 \times 10^8, \gamma_y = 0.76, \quad (5.11)$$

$$f = 64.43, c_b = 3.58, c_L = 0.36, k = 1.29, \tau = 0.074 \quad (5.12)$$

The results of this fitting procedure is shown in Fig. 5.2, showing an excellent agreement between the theory and experiment.

To get a deeper understanding of the underlying effect, we look at the evolution of the free energy surfaces for both order parameters, as shown in Fig. 5.3. The characteristic double well potential for $L \neq 0$ equilibrium is clearly visible, and as expected, when the pulses hit and T_L increases in the term $\alpha(T_L - T_c)L^2$ of Eq. 5.3, we see that the potential flattens causing the the minimum of L to very quickly change, as discussed above. This in turn causes the single-well potential of y to shift as quickly. The dynamics of y is orders of magnitude slower than that of L and due to this instant shift of the energy surface, it will cause an oscillation of y . While the temperature T_L decreases again, L and the

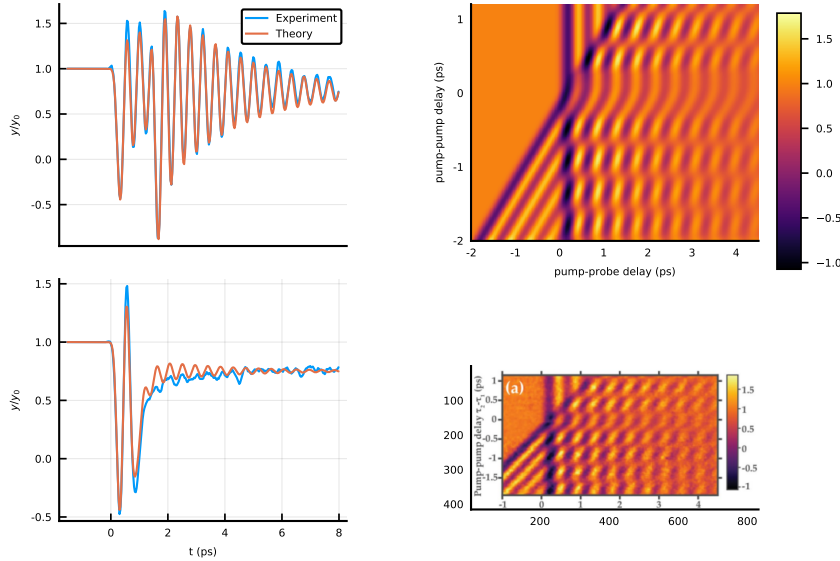


Figure 5.2: Comparison of theoretical fit vs Experiment. (a-b) Two examples of fits to constructive (a) and destructive (b) experiments. (c-d) Comparison of the theoretically generated heatmap (c) with the experimental heatmap (d).

minimum of the y potential shift back towards the original equilibrium position. The oscillation of y remains for a relatively long time while this shift is occurring since the damping is not that big (of the order of 4ps). It then becomes clear that if the second pulse can repeat this mechanism while the oscillation of y is still there, it can be increased or decreased depending on the timing. Having this understanding, let's investigate what the ideal way to excite y is.

First of all, when the system is relatively close to the phase transition of L , a small increase of temperature causes a large change in the value of L as shown through Eq. 5.9, and thus causes a large the shift of the potential for y . It is then important to keep this initial shift of the potential for y in place until y crosses the minimum, converting as much potential energy into "kinetic" energy. This requires L to be heated slightly above the PT, which leads to the largest possible shift of the potential of y , and the additional temperature of L above T_c , together with the non-infinite cooling rate, allows y to gain the maximum kinetic energy. Since only the size of L matters for the potential surface of y , it can only cause a shift in one direction, meaning that, similar to someone pushing a swing, the ideal intervals for the subsequent pulses are close to multiples of the period of y , if the goal is maximum oscillation amplitude. The amount of periods depends on the cooling rate of L , this influences how much T_L can cool back down within one period and thus the size of the maximum shift, since this depends on distance of T_L from T_c , and the damping of y since that is the main source of kinetic energy loss. Taking these understandings into consideration, a high degree of control of the oscillation of y can be achieved through the intensity, amount and timing of a pulse train applied to the material. To demonstrate this, we went one step further and utilized the fitted model to simulate what

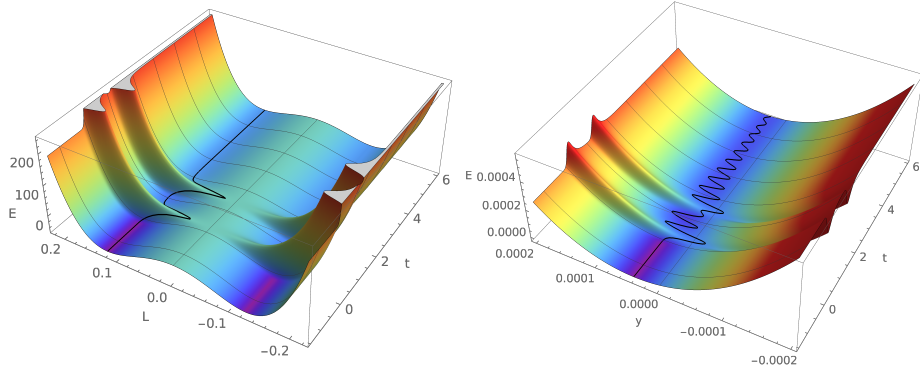


Figure 5.3: Time evolution of the energy surfaces of the order parameters.

pulse train has to be applied to the material in order for the oscillation maxima to follow a given envelope signal. To limit the dimensionality of the manifold of possible solutions, we performed the following ruleset:

- Only one fluence can be used per pulse
- Pulses are grouped in sets per period of oscillation
- The first pulse group only has a single pulse, applied 20 fs after the first non zero value of the envelope function, this determines the fluence of each pulse
- The maximum allowed pulses per group is fixed
- The groups are then fitted sequentially, since the later pulses don't influence the oscillation caused by the earlier ones
- If the function is seen to increase during a period, the pulses will be initiated close to the ideal boost location, and if a decrease is required, close to the ideal brake location

Adhering to these rules, we tested this procedure on different envelope functions, showcased in Fig. 5.4. One assumption made here was that the heat capacity of the bath c_b was increased to infinity, this is done because with the increase of temperature of the bath, the equilibrium position of L changes and leads to a general downwards slope of the oscillation of y as see from panel (a-b) of Fig. 5.2.

Having fit the model, we can go one step further and try to fit the PLD oscillation to an arbitrary signal shape. To this end we use the fitted model, and predict the timing of a fixed fluence pulse train that will result in the required shape. The results are shown in Fig. 5.4. This showcases that with an arbitrary pulse train we can achieve indirect, but optimal control of the PLD order parameter.

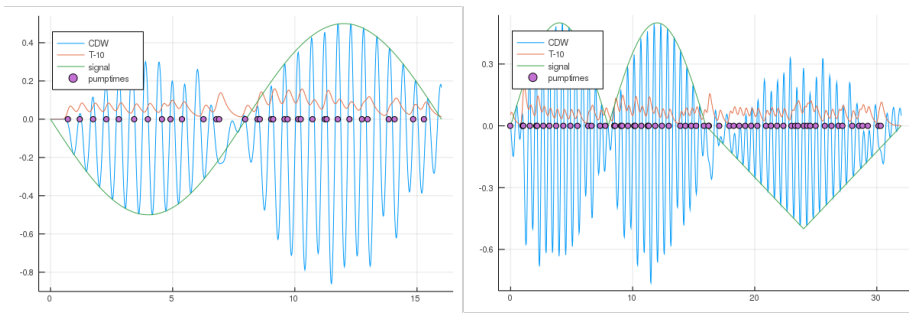


Figure 5.4: Two examples of optimal control. (a) Shows a reproduction of a sinusoidal envelope function, (b) shows the result for more complicated envelope, with an absolute value of a sinusoidal followed by a half a period of a sawtooth function. The pulse train is highlighted by the purple dots, and the evolution of the temperature of the SDW is given by the orange plot.

Chapter 6

Topological Multiferroic switching; coupling between Magnetism and Ferroelectricity in GdMn₂O₅

6.1 Introduction

[words to sprinkle around: coexist, attracted much attention] Efficient control and probing of robust order has historically been one of the main technological drivers for research in condensed matter. The hallmark example is the impact that the discovery of Giant Magnetoresistance has had on the efficiency of hard disks. By alternating the information storing (usually) ferromagnetic domains with nonmagnetic metallic domains, the ability to purely electrically read back information that was previously written was unlocked, leading to a great increase in the reading efficiency. This effect is based on the dependence of the electrical conductivity of ferromagnetic metals on the spin orientation of the current carriers, a beautiful example of the technological promises that the field of spintronics holds. There remains, however, the issue of writing the information in the first place. In current state of the art storage technologies from the point of view of density, this is still done by applying an external magnetic field with an electromagnet to reorient the ferromagnetic domains. One can imagine this to be quite an inefficient process, both from the point of view of granularity (stray fields and non-locality of the magnetic fields limit the minimum size of the domains) as from that of energetics. Improving these figures of merit drives much of the current research in the field of spintronics, with promising applications like spin-transfer torque devices, utilizing the torque applied by spin-polarized current carriers on the magnetic moments inside the storage medium, circumventing the need to create a magnetic field from circular currents. It is clear that the longevity of magnetism based order, combined with

the ease of manipulation associated with charge based order is highly desirable. This leads us to the topic of this chapter, namely the magnetoelectric effect in multiferroic insulators. As the name implies, the magnetoelectric effect allows for the electric control of magnetic order or the magnetic control of ferroelectric polarization[6, 4, 2, 3, 1], the former of which is most important for technological applications. In practice, however, there are many issues that limit the effectiveness of this cross-order coupling, and the number of multiferroic materials is limited to begin with. This latter point can be partly understood from a symmetry point of view. Namely, ferroelectric materials break inversion symmetry, whereas magnetic order needs the breaking of time reversal symmetry. There are thus only 13 Shubnikov magnetic point groups that allow simultaneous appearance of ferroelectricity and magnetization [8], but not all compounds that belong to one of those 13 groups showcase multiferroicity. Another reason for the relative sparseness of multiferroic materials is that, generally speaking, ferroelectricity and magnetism are not compatible on the ionic level, i.e. they require ions with different valence configurations. For example, in perovskites (ABO_3 , A cation, B anion), there are many ferroelectric or magnetic oxides, but the combination of the two is very uncommon. The reason in this case is that, in general, a prerequisite for ferroelectricity is a valence configuration of d^0 , i.e. an empty d -shell, or the presence of lone pairs (ns^2). Conversely, magnetism requires partially filled d or f shells, such that the unpaired electrons lead to nonzero magnetic moments on the constituent ions. It is clear that it is impossible to reconcile these two requirements simultaneously, thus making multiferroics not commonplace [*there is also the issue of hybridization where empty shells lead to occupation of bonding orbitals and half-filled orbitals engaging in anti-bonding hybridization never stabilizing the ionic shift, not sure if I should also discuss that*]. There are two ways around this issue, which lead to so-called Type-I and Type-II multiferroics[4]. The Type-I variety harbors two different ‘subsystems’ that separately handle either the magnetic or ferroelectric order. Referring back to the perovskites discussed above, one could, for example, imagine a ferroelectrically active A-site cation such as Bi^{3+} or Pb^{3+} , combined with a magnetically active B-site anion such as Fe [8]. This strategy gets around the issue of the mutual exclusivity of ferroelectricity and magnetization on the ionic level, and can lead to large magnitude of both orders [*specifics?*], but also tends to lead to small magnetoelectric effects due to the different origins of the two orders. Ideally, one uses the other variety, i.e. Type-II multiferroicity, where the magnetic and ferroelectric orders both originate from the same underlying physics. The usual situation in these Type-II materials is that one order stabilizes, lowering the symmetry of the material and thus allowing for the other to also appear. The key example that we discuss here is that of an inversion breaking magnetic configuration that leads to the appearance of ferroelectricity [*add more examples, show the symmetry considerations discussed in wang for spin-spirals?*]. Although the size of the electric polarization thus created is usually orders of magnitude smaller than in Type-I materials, the common origin of the two orders leads to a very sizable magnetoelectric effect. Here we specifically investigate GdMn_2O_5 (see Fig. 6.1), an example of a type-II multiferroic[4], where the ferroelectric polarization can be controlled to a high degree by the application of an external magnetic field, as will be shown below. Gd^{3+} is special with respect to the other rare-earths in the orthorhombic magnanites $RMn_2\text{O}_5$ (R being one of the rare-earths), because it

has a very isotropic electronic configuration ($4f^7$), i.e. there is no unquenched OAM and associated anisotropic charge distribution. This means that the large spin (nominally $S = 7/2$) can orient itself relatively freely to optimize the magnetic interactions with its neighboring Mn atoms. This turns out to be one of the main reasons behind the very large electric polarization and magnetoelectric coupling of GdMn_2O_5 , compared to other multiferroics, and even to other $RMn_2\text{O}_5$ compounds.

The orthorhombic manganites have a very complex crystalline structure, which leads to a wealth of different phases depending on the temperature, magnetic field and even electric-field poling history [9]. To keep the discussion tractable and in line with the experiments that were performed, we give a summary of the transitions and phases that are important for this part of the Thesis.

All orthorhombic manganites have space group $Pbam$ [**Alfonso97a**] in the paramagnetic phase at high temperature, which eventually gets lowered to P_ab2_1a when the commensurate magnetic order locks in below $T_N \sim 33K$. This order is characterised by the propagation vector $\mathbf{k} = (1/2, 0, 0)$, i.e. there is a unit cell doubling along the crystalline a direction. Spins are ordered ferromagnetically along the crystalline c direction. This magnetic transition goes hand in hand with a sharp anomaly in the dielectric constant ε_b , signalling the onset of the improper ferroelectric order along the b -direction [5]. When the temperature is lowered further, the polarization P_b saturates to a maximum value of around $3600\mu\text{C}/\text{m}^2$, which is the largest of all rare-earth manganites, but still tiny compared to proper ferroelectrics like BaTiO_3 with $P \sim 2 \times 10^5\mu\text{C}/\text{m}^2$. The magnetic configuration features two AFM Mn chains per unit cell, that feature both Mn^{3+} pyramids and Mn^{4+} octahedra, as indicated by the light blue lines and purple polygons in Fig. 6.1. The Mn spins of the chains in GdMn_2O_5 lie mostly along the easy axis of the Mn pyramids, making angles of $\pm 23.4^\circ$ with the a -axis. There are two sources of ferroelectricity as shown in Fig. 6.1 panels (b-c), both originate from symmetric exchange striction ??, where the AFM superexchange combined with the spin configuration will decrease the length of bonds with antiparallel spins, and increase those with parallel spins. The first of those contributions (panel b), P_{MM} , comes from the interchain (roughly along the b -direction) frustration between $Mn^{3+} - Mn^{4+} - Mn^{3+}$ ion sequences, the second (panel c), P_{GM} originates from the frustrated interaction between the Gd spins and neighboring Mn chains. Both of them result in both ionic (leading to the lower P_ab2_1a symmetry), and electronic contributions to the polarization. P_{MM} is also present in other $RMn_2\text{O}_5$ compounds, but it was shown that the electronic and ionic contributions are oriented in opposite sense and nearly cancel each other [4]. There is no such cancellation associated with P_{GM} , causing it to be the origin of the large P_b . Together with the large magnetic susceptibility caused by the size and isotropic nature of the Gd spins, this leads to GdMn_2O_5 outclassing the other $RMn_2\text{O}_5$ compounds both in size and tunability of P_b , with a measured variation of up to $5000\mu\text{C}/\text{m}^2$ when a magnetic field is applied ??.

Now that the stage is set, we continue describing the experimental observations that we will try to explain.

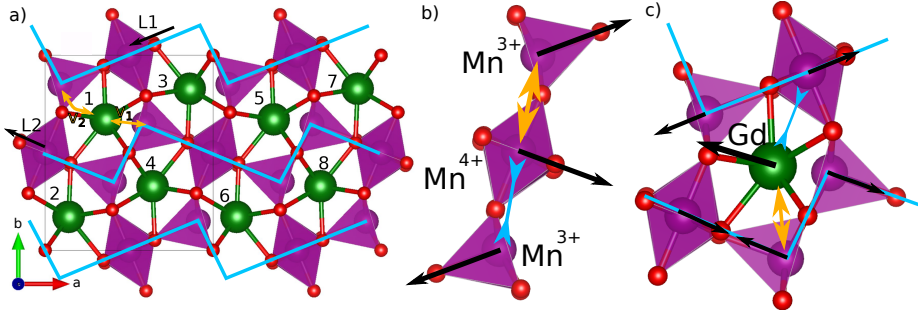


Figure 6.1: **Unit cell and magnetic configuration of GdMn_2O_5 .** The spheres signify Mn (purple), Gd (green) and Oxygen (red) ions. a) *Magnetic unit cell*, the zig-zag chains along the a -direction (cyan lines) show which Mn ions are linked with strong AFM exchange, resulting in the \mathbf{L}_1 and \mathbf{L}_2 Néel vectors. The boundary of the structural unit cell is marked by the black box and the yellow arrows denote the exchange paths between Gd and neighboring Mn ions in both chains, corresponding to v_1 and v_2 . (b-c) *Symmetric magnetostriiction*, the black arrows signify the zero field orientation of the spins. The yellow arrows denote the expanding bonds due to alignment of spins and AFM exchange, and the blue arrows denote contracting bonds.

6.2 Experimental results

In previous experimental measurements, the magnetic field was always applied along the crystalline a -direction ???. This leads to the aforementioned reversal and restoration of the polarization, and a relatively normal hysteresis loop (see Fig. 1 of [5]), alternating between two states. However, we found that the behavior of $P(H)$ depends strongly on the angle between the applied magnetic field and the a -direction, ϕ_H . As can be seen from Fig. 6.2 panel a, at high angle P_b remains positive although a small jump can be observed signalling two different internal states. In the intermediate ‘magic angle’ region (panel b and d), there is a crossover between the low angle regime of Ref. ?? and the high angle regime of our experiments, where four different states with different values of P_b are visited while the external field cycles up and down twice. This novel four state switching is the focus of this part of the thesis, and is found to originate from a rotational motion of the internal spins in one direction. One could say that this behavior is a microscopic analogy to the crankshaft in a car, converting the linear back-and-forth motion of the magnetic field into a unidirectional rotational motion of the spins. As will be shown below, these three regimes can each be assigned a winding number, with the four state switching regime lying on the boundary between the two extremal regimes. The topology of the parameter space in terms of ϕ_H is found to be such that this four state switching phase can be thought of as topologically protected, i.e. there always exists a region of ϕ_H where the four state cycle is present. The actual size of this region depends on the specific model parameters used, as will be discussed below. The results of the experiments performed on single crystal GdMn_2O_5 samples are shown in Fig. 6.2. As can be seen from the varying behaviors in panels (a-d), the evolution of P_b with $|H|$ is very dependent on its angle with the a -axis, ϕ_H . As alluded to before, at a certain magnitude of

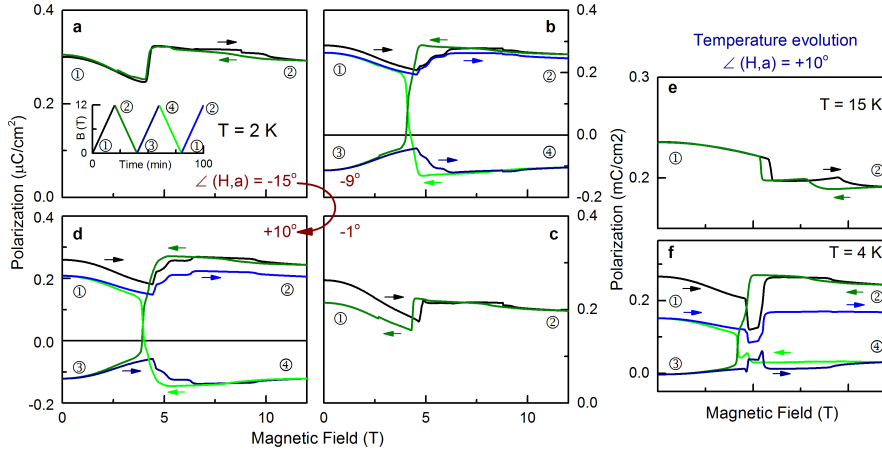


Figure 6.2: Evolution of the electric polarization loop across critical angle and critical temperature. (a) At higher temperatures only a small step is seen at the transition that shows some hysteresis and the two-state switching; (b) 4-state switching starts to appear approximately from $T = 5$ K. (c) four-state hysteresis loop is clearly seen at $T = 2.3$ K with the magnetic field at the “magic” angle; (d-f) Field dependence of the electric polarization of GdMn_2O_5 for different off-axis orientations of the applied magnetic field. (d,f): Conventional two-state switching is observed if magnetic field is (d) far away from the “magic” direction or (f) very close to the crystallographic a -axis. (e,g): Unusual four-state hysteresis loop for the magnetic field direction close to the magic angle of $\pm 9^\circ$. The inset shows the sequence of the magnetic field-sweeps. The labels 1-4 mark the four polarization states. The arrows show the direction of magnetic field-change during the sweep. The experiments have been done at $T = 2.3$ K.

this angle and at low temperature, a peculiar deterministic four-state hysteresis loop develops. Even though all experimental measurements were performed on single crystal samples, the complexity and low symmetry of the material leads to a wealth of different effects, which is clear from the details of the P_b evolution at $T = 4K$, shown in panel e, but also from some details of the evolution at $T = 2K$. We will only focus on the overall behavior, i.e. how the main four-state regime develops as an interpolation between the high and low angle regimes that have the more usual two state switching loop. It is not clear what led to the discrepancy between the present low angle measurements (panel a) and earlier ones performed in Ref. [5], from our theoretical model it will be shown that the behavior in Ref. [5] arises, rather than the one observed here.

6.3 Modeling

In order to describe the physics at play we use a quasi-classical model Hamiltonian with eight Gd spins designated by unit vectors $\mathbf{S}_i, i = 1..8$, two AFM order parameters $\mathbf{L}_\alpha, \alpha = 1, 2$ (also unit vectors) given by the difference of spins of neighboring Mn ions inside the two Mn chains, and the slave order parameter P_b

for the polarization, see Fig 6.1. Using these AFM order parameters amounts to taking the rigid spin approximation, i.e. all spins in each chain are assumed to be collinear with the same size and alternating sign. This simplification is justified by the large intrachain AFM exchanges, compared with the relatively small exchanges between the two chains. Another simplification that is adopted is to keep all spins in the *ab*-plane, since this was experimentally shown to be the case, and the layers couple ferromagnetically along the crystalline *c*-direction [5]. This lowers the dimensionality of the problem from 3D to 2D, with a single angle per Gd spin and Mn chain as the remaining degrees of freedom, greatly simplifying the numerical solution. Since all spins and AFM order parameters are unit vectors, their sizes are implicitly included in the model parameters.

The next step in deriving the appropriate model Hamiltonian using these simplifications and order parameters is to find symmetrically allowed combinations of them, which have to transform according to the unit representation of the symmetry group of the crystal. To this end we utilize the following symmetry operations of the paramagnetic high symmetry *Pbam* phase:

$$I : (x, y) \rightarrow (-x, -y) \quad (6.1)$$

$$2z : (x, y) \rightarrow (-x, -y) \quad (6.2)$$

$$2y : (x, y) \rightarrow (\frac{1}{2} - x, \frac{1}{2} + y) \quad (6.3)$$

I and *2z* are the same symmetry operations in the 2D case. Next, a doubling of the unit cell is necessary to fit the overall AFM magnetic state. This leads to additional symmetry operations when the spins are not taken into account, which in light of brevity we won't fully enumerate here. For our purposes it suffices to write *2y* : $(x, y) \rightarrow (\frac{1}{4} - x, \frac{1}{2} + y)$ and add an additional symmetry operation *a* : $(x, y) \rightarrow (x + a, y)$. In effect, applying these symmetry operations to the degrees of freedom, bearing in mind the AFM spin transformation between the two halves of the magnetic unit cell, leads to the following transformation table:

	S_1	S_2	S_3	S_4	S_5	S_6	S_7	S_8	L_1	L_2	P_b
<i>I</i>	S_8	S_7	S_6	S_5	S_4	S_3	S_2	S_1	$-L_1$	L_2	$-P_b$
<i>2y</i>	S_4	S_3	S_2	S_1	S_8	S_7	S_6	S_5	L_1	L_2	P_b
<i>a</i>	S_5	S_6	S_7	S_8	S_1	S_2	S_3	S_4	$-L_1$	$-L_2$	P_b

The first set of contributions are the Heisenberg exchange terms between the Gd spins and the Mn chains (L_1 and L_2), with the effective exchange parameters denoted by v_1 and v_2 . The former (latter) couples each Gd spin with the chain that harbors the closest (furthest) Mn ion. Starting from terms with S_1 and S_2 , taking into account the above table of transformations, the following sets of terms can be identified:

$$\begin{aligned} \mathbf{S}_1 \cdot (v_1 \mathbf{L}_2 + v_2 \mathbf{L}_1) &\xrightarrow{I} \mathbf{S}_8 \cdot (v_1 \mathbf{L}_2 - v_2 \mathbf{L}_1) \xrightarrow{a} \mathbf{S}_4 \cdot (-v_1 \mathbf{L}_2 + v_2 \mathbf{L}_1) \xrightarrow{I} \mathbf{S}_5 \cdot (-v_1 \mathbf{L}_2 - v_2 \mathbf{L}_1) \\ \mathbf{S}_2 \cdot (v_1 \mathbf{L}_1 + v_2 \mathbf{L}_2) &\xrightarrow{I} \mathbf{S}_7 \cdot (-v_1 \mathbf{L}_1 + v_2 \mathbf{L}_2) \xrightarrow{a} \mathbf{S}_3 \cdot (v_1 \mathbf{L}_1 - v_2 \mathbf{L}_2) \xrightarrow{I} \mathbf{S}_6 \cdot (-v_1 \mathbf{L}_1 - v_2 \mathbf{L}_2) \end{aligned} \quad (6.4)$$

The sum of all these contributions has the correct unit representation of energy,

leading to the first contribution to the Hamiltonian:

$$\begin{aligned} H_{LS} = & \mathbf{S}_1 \cdot (v_1 \mathbf{L}_2 + v_2 \mathbf{L}_1) + \mathbf{S}_2 \cdot (v_1 \mathbf{L}_1 + v_2 \mathbf{L}_2) + \mathbf{S}_3 \cdot (v_1 \mathbf{L}_1 - v_2 \mathbf{L}_2) + \mathbf{S}_4 \cdot (-v_1 \mathbf{L}_2 + v_2 \mathbf{L}_1) \\ & - \mathbf{S}_5 \cdot (v_1 \mathbf{L}_2 + v_2 \mathbf{L}_1) - \mathbf{S}_6 \cdot (v_1 \mathbf{L}_1 + v_2 \mathbf{L}_2) - \mathbf{S}_7 \cdot (v_1 \mathbf{L}_1 - v_2 \mathbf{L}_2) - \mathbf{S}_8 \cdot (-v_1 \mathbf{L}_2 + v_2 \mathbf{L}_1) \end{aligned} \quad (6.5)$$

Since P_b is a scalar, a similar process can be applied starting from $P_b \mathbf{S}_1 \cdot (\beta_2 \mathbf{L}_1 + \beta_3 \mathbf{L}_2)$ and $P_b \mathbf{S}_2 \cdot (\beta_2 \mathbf{L}_1 + \beta_3 \mathbf{L}_2)$, which signify the symmetric Heisenberg magnetostriction contribution to the Hamiltonian. This leads to

$$\begin{aligned} H_{P_b} = & -P_b [E_b + \beta_1(\mathbf{L}_1 \cdot \mathbf{L}_2) + (\mathbf{S}_1 - \mathbf{S}_5)(\beta_2 \mathbf{L}_2 + \beta_3 \mathbf{L}_1) + (\mathbf{S}_2 - \mathbf{S}_6)(\beta_2 \mathbf{L}_1 + \beta_3 \mathbf{L}_2) \\ & + (\mathbf{S}_3 - \mathbf{S}_7)(\beta_2 \mathbf{L}_2 - \beta_3 \mathbf{L}_1) + (\mathbf{S}_4 - \mathbf{S}_8)(\beta_2 \mathbf{L}_1 - \beta_3 \mathbf{L}_2)], \end{aligned} \quad (6.6)$$

where the dipole term from a possible external electric field $P_b E_b$ was also included. A further three terms in the Hamiltonian depend solely on L_1 and L_2 :

$$H_L = \Gamma(\mathbf{L}_1 \cdot \mathbf{L}_2)^2 + \sum_{\alpha} \chi^{-1}((\mathbf{H} \cdot \mathbf{L}_{\alpha})^2 - H^2) - K_L \sum_{\alpha} (\mathbf{L}_{\alpha} \cdot \mathbf{n}_{\alpha})^2 \quad (6.7)$$

The first originates from the gain in exchange energy through spin canting when the chains are not colinear, due to the competition of interchain exchange J_{\perp} and the intrachain AFM exchange J_{\parallel} [7] [more details?], with $\Gamma \sim \frac{J_{\perp}^2}{J_{\parallel}} > 0$. The term with χ represents the gained Zeeman energy when the Mn spins are slightly canted from the purely AFM order inside the chains, resulting in a weak magnetic moment which couples to the external field. The last denotes the easy-axis anisotropy which is aligned with the fourfold axes of the pyramidal coordinated Mn ions, i.e. $\mathbf{n}_{\alpha} = (\cos(\pm 23.4^\circ), \sin(\pm 23.4^\circ))$ respectively.

Similarly, three terms can be identified as coming purely from the Gd spins:

$$H_S = \frac{1}{2}(g\mu_B)^2 \sum_{i \neq j} \left(\frac{\mathbf{S}_i \cdot \mathbf{S}_j}{r_{ij}^3} - 3 \frac{(\mathbf{S}_i \cdot \mathbf{r}_{ij})(\mathbf{S}_j \cdot \mathbf{r}_{ij})}{r_{ij}^5} \right) - \sum_i (K_S(\mathbf{N}_i \cdot \mathbf{S}_i)^2 + g\mu_B \mathbf{H} \cdot \mathbf{S}_i) \quad (6.8)$$

The first describes the magnetodipolar interaction between Gd spins, which could be relatively large due to the size of the spins and relative proximity to the neighbors. In the numerical simulations these were restricted to five nearest neighbors, including periodic images. Including further neighbors did not lead to qualitative differences of the results. Again an anisotropy term is included, this time with anisotropy axes N_i , unit vectors alternating as $\pm 12^\circ$. K_S is significantly smaller than K_L due to the isotropic environment and spin configuration of the Gd ions. The final term denotes the Zeeman energy from the interaction with the externally applied magnetic field.

The model parameters used here are $J_{\perp} = 1.89$ meV, $J_{\parallel} = 26.67$ meV, $K_L = 5.27$ meV, $K_S = 0.2$ meV, $v_1 = 3.33$ meV, $v_2 = 0.15$ meV [check order parameters, maybe show different sets?]. with the model parameters used to fit the experimental data, $\alpha = 0.06 \mu\text{C}/\text{cm}^2$, $\beta = 0.04 \mu\text{C}/\text{cm}^2$, $\gamma = 0.06 \mu\text{C}/\text{cm}^2$.

As mentioned before, the low temperature commensurate state breaks both time reversal symmetry, $T : (\mathbf{L}_1, \mathbf{L}_2) \rightarrow (-\mathbf{L}_1, -\mathbf{L}_2)$, and inversion symmetry $I : (\mathbf{L}_1, \mathbf{L}_2) \rightarrow (-\mathbf{L}_1, \mathbf{L}_2)$, leading to a fourfold degenerate energy surface as shown in Fig. ???. To simulate the experimental measurements in Fig. 6.2 at low

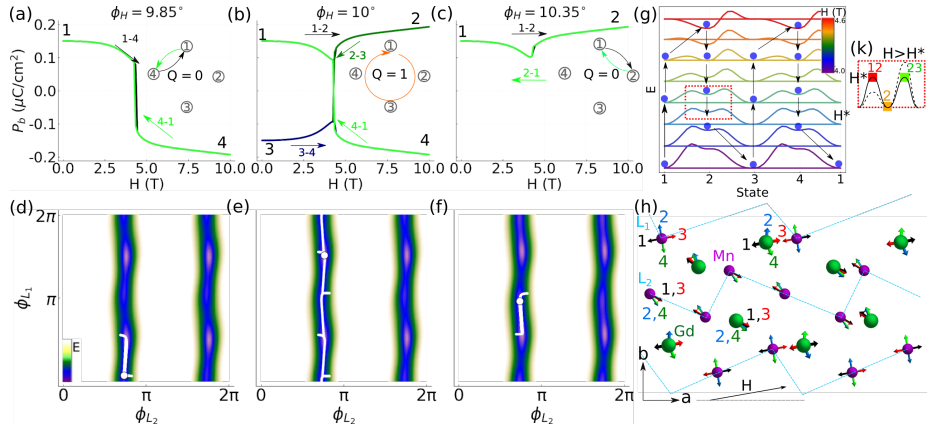


Figure 6.3: Simulation of magnetoelectric behaviour. (a-c) Evolution of electric polarization P_b during the magnetic field sweep cycle for various magnetic field orientations. In each panel, the changes of the curve color indicate the same progression of the sweep cycle as Fig 2. The four-state switching is seen for the field at the magic orientation. The insets indicate the corresponding switching paths and winding numbers. (d-f) Trajectories (in green) in the space of the Néel vectors orientations, (ϕ_{L_1}, ϕ_{L_2}) , through the field sweep cycles in different regimes. The color map shows the energy landscape in the vicinity of the switching fields. (g) Evolution of transition barriers between states 1,2,3,4 as the magnetic field at 10° to the a axis is swept through the hysteresis region. The plots are shifted vertically, and magnetodipolar interactions were enhanced by a factor of 5.3 for clarity. The curve colors encode the corresponding magnetic field strength. The trajectory of the energy minimum due to field sweeps is shown with blue circles and arrows. Coordinated changes of the state energies and barrier asymmetry with magnetic field enable the topological behavior. (h) Spin configurations in states 1, 2, 3 and 4. (k) Schematic evolution of the barriers connecting the state 2 to states 1 and 3 in the vicinity of H^* . Saddle point states are denoted by 12 and 23.

temperature, we choose one of the four degenerate minima of the Hamiltonian, gradually increase and decrease the applied magnetic field, and minimize the energy in order to track the instantaneous local minimum.

The results are shown in Fig. 6.3

In order to understand the energy surface connecting the four states, we proceed by labeling them in the same way as Fig. 6.2, and perform a nudged elastic band calculation between the four states at a given magnetic field inside the hysteresis region. This results in the evolution of barriers between these states as shown in panel (g), where the color coding is used to denote the magnetic field strength, and the energy graphs are offset for clarity. The arrows and blue balls denote the evolution during the double magnetic field sweep. As expected, two minima with opposite P_b are degenerate each value of H , at low field these are located at states 1 and 3, then as the field is ramped up they move to favor states 2 and 4. We see that during the sweep the barriers between the different states evolve asymmetrically. Starting in state 1, when the field is ramped up the barrier towards state 2 decreases faster than the one

towards state 4, causing the system to move from 1 to 2. Then, as the magnetic field is lowered again, the barrier from 2 to 3 increases slower than from 2 to 1. When ultimately state 2 goes from being metastable to a saddle point, the system spills over towards state 3, and so on. In order to try and understand where the asymmetric evolution of the barriers comes from, we investigate the situation around the particular H -field strength where the system is close to state 2, and the barriers between state 2 and 1, and 2 and 3 are the same height. This situation is highlighted by the red dashed box around the blue graph in Fig. 6.3(g). The inset of panel (k) provides a zoom on the energy surface. The states 12 and 23 denote the configurations on top of the barriers from 1 to 2 and 2 to 3, respectively. A Taylor expansion in terms of H , around H^* can be performed for both states:

$$F(H) = F(H^*) + \frac{\partial F}{\partial H} \Big|_{H=H^*} (H - H^*) + \dots \quad (6.9)$$

If one then subtracts the results, using $\frac{\partial F}{\partial H} = M$, the following expression is found

$$E_{12}(H) - E_{23} \sim (M_{12} - M_{23})(H - H^*). \quad (6.10)$$

This means that, to first order, the evolution of the barrier asymmetry is given by the difference in magnetization of the two states on top of the barriers. The magnetization of both states can be calculated using the following formula

$$\mathbf{M} = -\frac{\partial F}{\partial \mathbf{H}} = \sum_i g\mu_B \mathbf{S}_i - \sum_\alpha 2\chi^{-1} \mathbf{L}_\alpha (\mathbf{H} \cdot \mathbf{L}_\alpha) \quad (6.11)$$

Indeed we find that the magnetizations are different from our simulations, $M_{23} > M_{12}$, confirming that this is at least a part of the reason for the asymmetric evolution of the barriers. Moreover, due to the symmetry of the system, this asymmetry is opposite when the field is swept up, as compared with when the field is swept down. This causes that when $H > H^*$ the barrier from state 1 to state 2 lowers faster than the one towards state 4, and by symmetry, the barrier from state 3 to state 4 lowers faster than from state 3 to 2. The converse is true when $H < H^*$, but since the system is then coming from the high-field configurations, it moves from 2 to 3 and 4 to 1 rather than the opposite direction. This causes the deterministic unidirectional movements through the four states sequentially when two field sweeps are applied. Since the two low field states that get accessed sequentially have two different P_b values, this situation effectively results in a single crystal binary counter behavior.

The magnetic configuration of the four extremal states is displayed in panel (h) of the same figure, showcasing the rotational motion of the spins inside the chain most parallel to the applied magnetic field, and the Gd ions coupled most strongly with it. This robust one directional rotation allows us to assign a non-zero winding number to the ‘magic-angle’ switching behavior, i.e. $Q = \frac{1}{2\pi} \int_0^{T_0} dt (L_x \partial_t L_y - L_y \partial_t L_x)$.

6.4 Simplified Model

Having found a description for the situation in the complicated material GdMn_2O_5 using the model ??, one may wonder what the minimal requirements are to have

a similar four-state behavior where the spins rotate 360° while the applied field only oscillates back and forth along a single axis. We look to the spin configurations of Fig. 6.3(h) for inspiration. It is clear that, although both chains are necessary for the P_b behavior, the chain with equilibrium Mn moments most parallel to the applied field does the full rotation, while the other chain merely oscillates around its starting position. Similarly, only the Gd moments most strongly coupled to that chain perform the full 360° cycle. This warrants an attempt to search for the four state behavior using only a single chain with its Gd moments, more specifically, in the case of $\phi_H = +10^\circ$, we keep L_1, S_2, S_3, S_6 and S_7 as the degrees of freedom in the model. Given the negligible importance of the anisotropy on the Gd ions, we also put $K_S = 0$. This leaves us with the following Hamiltonian, which is split up in two parts, one with the dipolar terms H_{dip} and one with all the other terms H' :

$$H = H' + H_{dip} \quad (6.12)$$

$$H' = v_1(\mathbf{S}_2 + \mathbf{S}_3 - (\mathbf{S}_6 + \mathbf{S}_7)) \cdot \mathbf{L}_1 - g\mu_b(\mathbf{S}_2 + \mathbf{S}_3 + \mathbf{S}_6 + \mathbf{S}_7) \cdot \mathbf{H} \quad (6.13)$$

$$- K_L(\mathbf{L}_1 \cdot \mathbf{n})^2 \quad (6.14)$$

$$H_{dip} = \frac{1}{2}(g\mu_B)^2 \sum_{i \neq j} \left(\frac{\mathbf{S}_i \cdot \mathbf{S}_j}{r_{ij}^3} - 3 \frac{(\mathbf{S}_i \cdot \mathbf{r}_{ij})(\mathbf{S}_j \cdot \mathbf{r}_{ij})}{r_{ij}^5} \right). \quad (6.15)$$

Due to the higher symmetries of this model throughout the field sweep cycle, compared with the full model, one can identify two symmetry related copies of one spin in the first half of the magnetic unit cell and one in the second half of the unit cell, with the chain in between (see Fig. 6.4), i.e. $S_2 = S_3$ and $S_6 = S_7$. This further simplifies the Hamiltonian:

$$H' = 2v_1(\mathbf{S}_3 - \mathbf{S}_6) \cdot \mathbf{L}_1 - 2g\mu_b(\mathbf{S}_3 + \mathbf{S}_6) \cdot \mathbf{H} \quad (6.16)$$

$$- K_L(\mathbf{L} \cdot \mathbf{n})^2 \quad (6.17)$$

$$H_{dip} = (g\mu_B)^2 \left(\frac{\mathbf{S}_3 \cdot \mathbf{S}_6}{r_{36}^3} - 3 \frac{(\mathbf{S}_3 \cdot \mathbf{r}_{36})(\mathbf{S}_6 \cdot \mathbf{r}_{36})}{r_{36}^5} \right). \quad (6.18)$$

[what can we say more about this?]

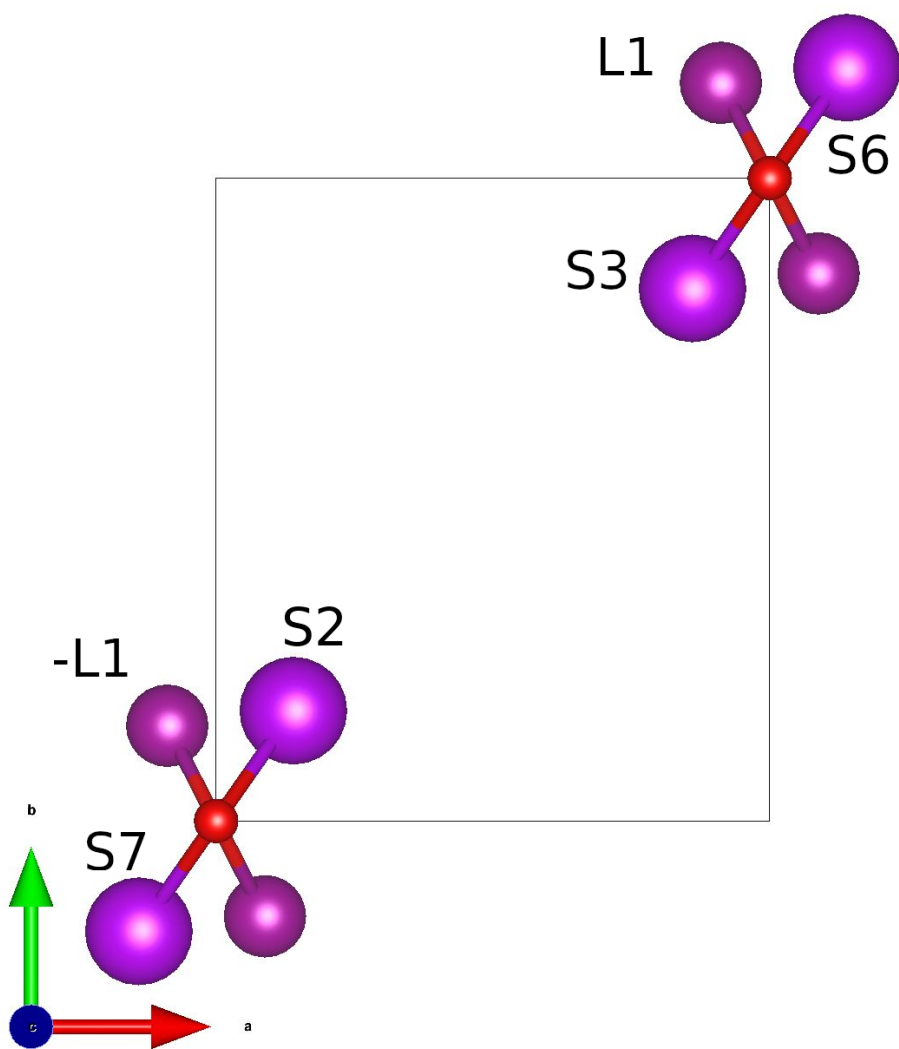


Figure 6.4: Simplified single chain model.

Bibliography

- [1] Sang-Wook Cheong and Maxim Mostovoy. “Multiferroics: a magnetic twist for ferroelectricity”. In: *Nature Materials* 6.1 (2007), pp. 13–20. ISSN: 1476-4660. DOI: 10.1038/nmat1804. URL: <https://doi.org/10.1038/nmat1804>.
- [2] Manfred Fiebig. “Revival of the magnetoelectric effect”. In: *Journal of Physics D: Applied Physics* 38.8 (2005), R123–R152. DOI: 10.1088/0022-3727/38/8/r01.
- [3] Manfred Fiebig et al. “The evolution of multiferroics”. In: *Nature Reviews Materials* 1.8 (2016), p. 16046. ISSN: 2058-8437. DOI: 10.1038/natrevmats.2016.46. URL: <https://doi.org/10.1038/natrevmats.2016.46>.
- [4] Daniel Khomskii. “Classifying multiferroics: Mechanisms and effects”. In: *Physics* 2 (2009), p. 20. DOI: 10.1103/Physics.2.20.
- [5] N. Lee et al. “Giant Tunability of Ferroelectric Polarization in GdMn_2O_5 ”. In: *Phys. Rev. Lett.* 110 (13 2013), p. 137203. DOI: 10.1103/PhysRevLett.110.137203.
- [6] N. A. Spaldin and R. Ramesh. “Advances in magnetoelectric multiferroics”. In: *Nature Materials* 18.3 (2019), pp. 203–212. ISSN: 1476-4660. DOI: 10.1038/s41563-018-0275-2. URL: <https://doi.org/10.1038/s41563-018-0275-2>.
- [7] A B Sushkov et al. “Electromagnons in multiferroic RMn₂O₅ compounds and their microscopic origin”. In: *Journal of Physics: Condensed Matter* 20.43 (Oct. 2008), p. 434210. DOI: 10.1088/0953-8984/20/43/434210.
- [8] K. F. Wang, J. M. Liu, and Z. F. Ren. “Multiferroicity: The coupling between magnetic and polarization orders”. In: *Advances in Physics* 58.4 (2009), pp. 321–448. ISSN: 00018732. DOI: 10.1080/00018730902920554. arXiv: 0908.0662.
- [9] S. H. Zheng et al. “Abnormal dependence of multiferroicity on high-temperature electro-poling in GdMn_2O_5 ”. In: *J. Appl. Phys.* 126.17 (2019). ISSN: 10897550. DOI: 10.1063/1.5120971.

Chapter 7

Mechanical softening in Ferroelectric domain walls

7.1 Introduction

The study of domain walls in ferroelectric and ferroelastic materials has taken the center stage in recent years. This is because they signify crossover regions between domains where the parent symmetry of the material was broken. These regions therefore often harbor effects that are markedly different from the behaviors found in the domains themselves. Here we investigate mainly 180° domain walls in ferroelectric BaTiO₃ (BTO). These domain walls are purely ferroelectric, i.e. the strain textures accompanying the ferroelectricity (see below for a more in depth discussion) is the same in both domains, separated by the wall. Given this fact it is fairly remarkable that it was observed that these walls are mechanically distinct from the domains they separate. In the case of BTO, they appear softer. After giving an overview of the performed experiments and the results we are trying to describe, we continue with a description of the underlying theory, followed by the numerical results together with a discussion.

7.2 Experimental

In order to characterise the stiffness of the material, scanning probe microscopy experiments were performed on single crystal BTO, by the group of Prof. Catalán. More specifically, Contact Resonance Frequency Microscopy (CR-FM) was performed, whereby an Atomic Force Microscopy (AFM) tip is brought into contact with the material, upon which the resonance frequency is measured. The higher the frequency the stiffer is the material in contact with the tip. This allows one to produce a mapping of stiffness the entire crystalline surface where the main limit on resolution is time. This leads to images as shown in Fig. 7.1, where there is a clear contrast between soft areas close to the wall and harder areas inside the domains. The softening of domain walls was previously studied for ferroelastic materials (i.e. materials where the wall separates two domains with different strain textures), where a similar effect was observed [1].

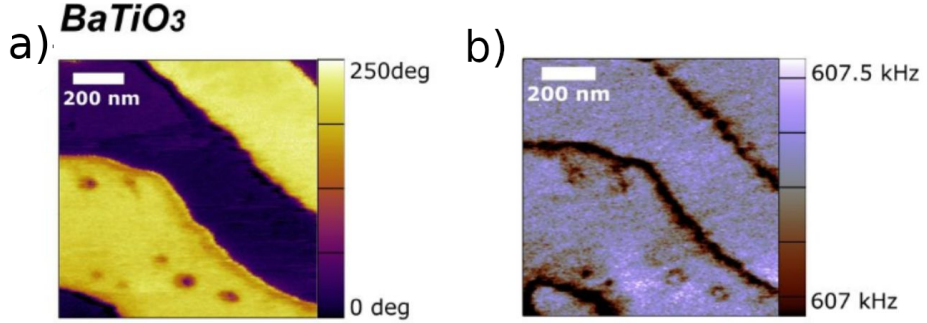


Figure 7.1: Ferroelectric polarization and stiffness maps of the surface of a single crystal of BTO. a) orientation of the ferroelectric polarization, obtained by Piezoresponse Force Microscopy (PFM). b) Mechanical response of the material as measured by CR-FM.

7.3 Theory

In order to describe the coupling between the ferroelectric order parameter P and the strain ε we use a Ginzburg-Landau-Devonshire model as described in [2]. The free energy density throughout the material is given by:

$$f = f_L + f_G + f_c + f_q + f_{fl}, \quad (7.1)$$

$$f_L = \alpha_{ij} P_{ij} + \frac{1}{2} \alpha_{ijkl} P_i P_j P_k P_l + \alpha_{ijklmn} P_i P_j P_k P_l P_m P_n, \quad (7.2)$$

$$f_G = \frac{1}{2} G_{jklm} \partial_k P_j \partial_m P_l, \quad (7.3)$$

$$f_c = \frac{1}{2} \varepsilon_{jk} C_{jklm} \varepsilon_{lm}, \quad (7.4)$$

$$f_q = -\frac{1}{2} \varepsilon_{jk} q_{jklm} P_l P_m, \quad (7.5)$$

$$f_{fl} = \frac{1}{2} f_{jklm} (\varepsilon_{jk} \partial_m P_l - P_l \partial_m \varepsilon_{jk}) \quad (7.6)$$

where the indices run through x, y, z , and einstein summation is assumed. The first term is the Landau free energy for a uniform ferroelectric polarization. Up to sixth order had to be included to bound the energy, since in BTO the fourth order term turns out to be negative. The second term denotes the Ginzburg part, the energy penalty occurred by spatial variations of the polarization. f_c is the elastic energy density, and f_q gives the contribution of electrostriction to the free energy. This is the main term coupling the polarization to the strain and causes the domains to be stretched along the polarization [add some panels like in the discussion of the powerpoint]. Lastly we include the flexoelectric contribution, f_{fl} , since it leads to small but possibly important effects.

The first possible source for the mechanical softening originates from the electrostriction term, and the strain texture it results in. As mentioned before, electrostriction stretches the domains in the direction of the polarization. Since we are investigating 180° domain walls, we can take the main polarization to be P_z , leading to a stretching of the domains in the z direction, or equivalently, $\varepsilon_{zz} \neq 0$ inside the domains. In the domain wall, however, P_z^2 is diminished and

even zero at the center. This then causes ε_{zz} to be diminished, but never reduced to zero due to compatibility relations and the elastic coupling to neighboring unit cells. Nonetheless, this will result in an indentation that forms at the location of the domain wall, as shown pictorially in Fig. 7.2(b), and more realistically in (c-d). As it turns out, the strain texture of this indentation stretches out relatively far [actual derivation and formula for this?] from the domain wall. This long-rangedness of strain is a general phenomenon, and depends on the morphology of the strain defect [more indepth on this?]. When the tip is then applied in an area where this strain texture is present, the wall will try to bend towards the tip in order to gain on the displacement. This will thus lead to a relatively big displacement to be caused by applying the tip, making the material appear soft.

Even though the interaction between the pinning potential, Peierls-Nabarro barriers, and electrostatics, with the force applied by the tip is hard to analytically describe, we can make statements about two extremes of the behavior: i) If the force of the tip is large enough, the wall slide towards it, maximizing the possible energy gain from the interaction with the tip. ii) A bending of the wall, where it remains inside the original Peierls-Nabarro potential, but deviates from the equilibrium position. [The situation that happens in the real material is more like a mix between the two, the top part of the wall bends almost completely towards the tip, but it's not moved as a whole because the bottom/bending electrostatics pins it. Can we say that these things are causing the potential for the entire wall to behave like the one we describe below?]

The first case can be ignored because this would mean that in the experiments, the wall would be dragged along the tip since the tip moves at a relatively slow rate, which would lose any contrast between wall and domain during the full measurement. We therefore try to formulate a simple free energy expansion for the second situation, where we assume that the wall at x_{DW} is pinned by a parabolic potential, and perturbed by a tip applying a force F_z at x_{tip} ,

$$E = E_0 - F_z u_z(x_{tip} - x_{DW}) + \frac{m\omega^2 x_{DW}^2}{2}. \quad (7.7)$$

We can expand this equation under the assumption of a small x_{DW} , i.e. that the wall doesn't move far from the $x_{DW} = 0$ equilibrium situation. Together with minimizing the energy we obtain $x_{DW} = -Fu'(x_{tip})/(m\omega^2)$, with a compliance correction $\Delta c = u'(x_{tip})^2/(m\omega^2)^2$. Thus, we can conclude that to maximize the softening, the tip should be applied where $u'(x_{tip})$ is large, i.e. within the strain variation caused by the above discussed electrostrictive coupling. This part of the effect is pictorially depicted in panel (b) of Fig. 7.2.

7.4 Results

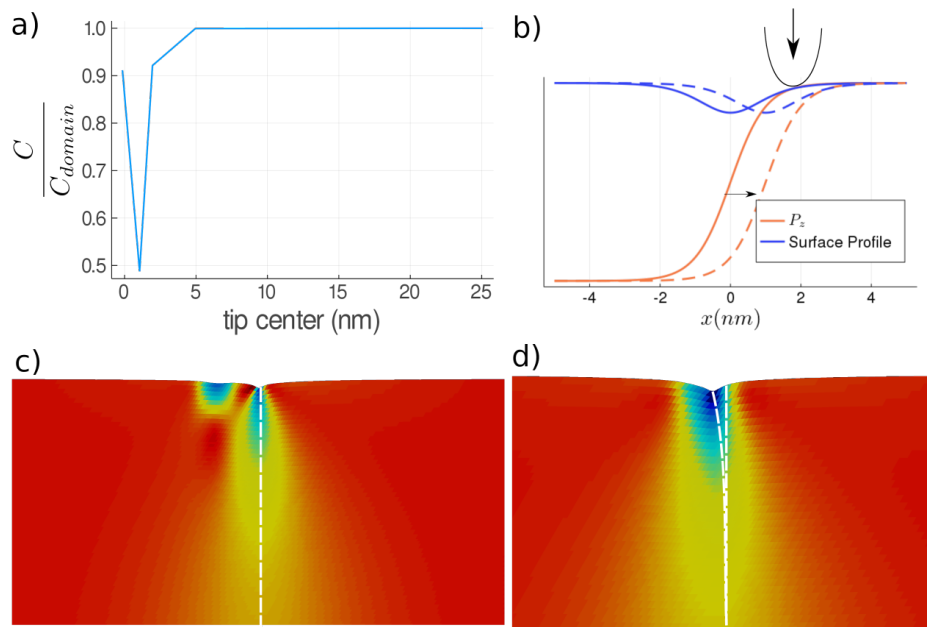


Figure 7.2

Bibliography

- [1] W T Lee, E K H Salje, and U Bismayer. “Domain wall diffusion and domain wall softening”. In: *J. Condens. Matter Phys.* 15.8 (2003), p. 1353.
- [2] P. Marton, I. Rychetsky, and J. Hlinka. “Domain walls of ferroelectric Ba-TiO₃ within the Ginzburg-Landau-Devonshire phenomenological model”. In: *Phys. Rev. B* 81.14 (2010), p. 144125.